TIME REVERSAL MICROWAVE METHODS FOR SOLVING INVERSE PROBLEMS IN NON-DESTRUCTIVE EVALUATION

By

Solimar Reyes Rodriguez

A DISSERTATION

Submitted to
Michigan State University
in partial fulfillment of the requirements
for the degree of

DOCTOR OF PHILOSOPHY

Electrical and Computer Engineering

2011

ABSTRACT

TIME REVERSAL MICROWAVE METHODS FOR SOLVING INVERSE PROBLEMS IN NON-DESTRUCTIVE EVALUATION

By

Solimar Reyes Rodriguez

Non-Destructive Evaluation (NDE) methods are use to inspect a material and components without damaging their usefulness. NDE is used in different industries to inspect the reliability of critical components, product quality, or detect material failure. The techniques used in NDE range from simple visual methods to microwaves,ultrasound, x-rays, and thermography. The key problem in NDE is the inverse problem which involves reconstructing defect profiles using the information in the output signal of the system. Inverse problem solutions in NDE can be classified as model-based and system-based approach. In model-based approach, an accurate forward model is used in an iterative framework to estimate the defect shape that minimizes the error between the measured and simulated signals. However, this approach results in repeated executions of a three dimensional forward model in each iteration, making it computationally demanding.

This thesis presents a direct approach to inversion using principles of time reversal. Time reversal focusing is based on the fact that when a wave solution is reversed in time and back propagated it comes to focus at the source. Research on time reversal techniques of ultrasound fields has demonstrated the reliability of the technique for detecting small defects in complex geometries. This thesis uses a computational model to study the feasibility of applying principles of time reversal to microwave NDE data for solving the inverse problem of defect detection in dielectric materials.

Microwave NDE methods are well suited for inspection of dielectric materials because electromagnetic waves can propagate through and interact with such materials. The interaction is influenced by the electrical and magnetic properties of the material

and hence the response of this interaction contains information of discontinuities of permittivity in the material.

A two-dimensional finite difference time domain (FDTD) model, for simulating the propagation of forward and time reversed wave fields is developed. A dielectric slab used in the simulations is illuminated by a gaussian modulated pulse. The measured microwave NDE measurements are recorded, time reversed and propagated backwards once through the FDTD model to highlight the scatterer/defect. Maxima in the energy image indicates the location of the defect. Simulation results demonstrate the ability of the technique to accurately detect defects in dielectric and lossy dielectric materials. Experiments were performed in free space to validate the FDTD model. The signals recorded in the experiment were time reversed and input to the FDTD model. Errors in source position, using the model, were attributed to experimental measurements.

DEDICATION

This thesis is dedicated to my husband Carlos Eduardo Nino Baron. He offered me unconditional love and support through my Ph.D. studies. I also dedicate this thesis to my parents Samuel Reyes Saldana and Aida Rodriguez Rodriguez for all their support, love and for teaching me the importance of education.

ACKNOWLEDGMENT

Different people helped me complete my Ph.D. degree. First of all, I have to thank my advisor, Dr. Lalita Udpa for all her invaluable guidance through my research, course work, and writing. I would also like to thank my graduate studies committee: Dr. Robert McGough, Dr. Satish Udpa, Dr. Wright, and Dr. Rothwell for their time, guidance and suggestions. Special thanks to Dr. Rothwell, who let me used his laboratory and equipment to perform the experiments that were necessary to complete this thesis and for his guidance after the experiments were completed.

I would also like to thank Benjamin Crowgey for all his time and for his help with the experiments. He taught me how to use the equipment and helped me with the experimental set up. I like to thank Raoul Ouedraogo for his help analyzing the experimental data.

Next, I would like to thank Dr. Barbara O'Kelly, Dr. Percy Pierre, the Sloan foundation, and the Graduate School for all their support, guidance, and funding through my graduate studies. I am a Harriet G. Jenkins Fellow and this fellowship provided me with funding for my graduate studies. I would like to thank this program for all the financial support and all the wonderful experiences that I was exposed to while being part of this program. I was also a Co-op student at NASA Glenn Research Center. The center provided me financial support over the summers and invaluable work experiences. I will always be grateful for the opportunities that the center gave me.

Finally, I would like to thank my parents, my friends, colleges at the MSU NDE laboratory and my beloved husband, Carlos Eduardo Nino Baron for all their support. They were with me every step of this incredible journey and I will always be grateful.

TABLE OF CONTENTS

List of Figures viii

1 Introduction **1**
1.1 Introduction to Non-Destructive Evaluation 1
1.2 Microwave NDT/NDE principles 3
1.3 Forward and Inverse Problem 6
1.4 Model-Based Approach 8
1.5 Time Reversal approach for inverse problems 9
1.6 Contributions 10

2 Forward Model **11**
2.1 Introduction 11
2.2 Maxwell Equations 11
2.3 FDTD Spatial and Time Discretization 15
2.4 Absorbing Boundary Conditions 18
2.5 Source 19

3 Inverse Problem Solution Using Time Reversal Techniques . . . **21**
3.1 Introduction to Inverse Problems in NDE/NDT 21
3.1.1 Calibration Techniques 21
3.1.2 Direct Methods 22
3.1.3 Indirect Inversion 23
3.2 Previous Research: Time Reversal Technique used in Ultrasound and Microwaves 24
3.3 Previous Research: Time Reversal Used to Solve the Inverse Problem 26
3.4 Proposed Approach to Solve the Inverse Problem in NDE/NDT: Time Reversal Technique using an FDTD Model 27
3.4.1 Mathematical Background 27
3.4.2 Time Reversal Focusing 29

4 Results **31**
4.1 Validation of Time Reversal Analysis 31
4.2 Application of Time Reversal for Defect Imaging 32
4.3 Test 1: Two scatterers in Dielectric Medium 34
4.4 Test 2: Single perfect electric conductor (PEC) Scatterer in Dielectric Medium 36
4.5 Test 3: Two Scatterers in Dielectric Medium- Resolution of the Model 36
4.6 Test 4: Two Scatterers in Dielectric Medium - Reconstruction with noise 37
4.7 Test 5: Two Scatterers in Dielectric Medium- Two Sources with Noise. 39

4.8 Test 6: Minimum number of sensors. 40
4.9 Test 7: Time Reversal Applied to Lossy Dielectric Medium. 43
4.9.1 Two well separated defects. 43
4.9.2 Closely placed defects. 47
4.10 Test 8: Effect of errors in receiver measurements. 53
4.10.1 Error in time measurements. 53
4.10.2 Error is Transducer Position. 56
4.11 Test 9: Results with different sensor locations 57
4.12 Test 10: Distances from the source to the sensor array. 61

5 Experiment **67**
5.1 Experiment Set Up 67
5.2 Experiment Calibration 70
5.3 Experiment Results 71

6 Conclusions **85**

7 Future Work **87**

Bibliography **90**

LIST OF FIGURES

1.1 General NDT/NDE system 2

1.2 Inverse problem description 7

1.3 Forward problem description. (a) Forward problem classified as the direct problem. (b) Forward problem classified as the signal detection problem. 8

1.4 Iterative process to solve the inverse problem 9

2.1 Spatial Grid for the FDTD algorithm. 16

2.2 FDTD Time Discretization Scheme. 17

3.1 Model based iterative method to solve the inverse problem. 24

4.1 Time reversal cavity that shows the receiver array location and the propagation of the Gaussian pulse. "For interpretation of the references to color in this and all other figures, the reader is referred to the electronic version of this dissertation." 32

4.2 Progress of electric field as a function of time when the electric field is propagated backwards in the model. 33

4.3 A block diagram indicating the procedure that was followed. 34

4.4 Simulations results for two scatterers in a dielectric medium. (a) Forward propagating wave from source. (b) Focusing of time reversed wave on scatterers. (c) Energy images indicating defects location. . . 35

4.5 Simulations results for single PEC scatterer in a dielectric medium. (a) Forward propagating wave from source. (b) Focusing of time reversed wave on scatterer. (c) Energy image indicating defect location. 37

4.6 Simulations results for 2 scatterers in a dielectric medium 2.27λ apart. (a) Focusing of time reversed wave on scatterers. (b) Energy image indicating location of defects. 38

4.7 Simulations results for 2 scatterers in a dielectric medium 6.28λ apart with noise. (a) Focusing of time reversed wave on scatterers. (b) Energy image indicating location of defects. 39

4.8 Simulations results for 2 scatterers in a dielectric medium 6.28λ apart with noise. (a) Focusing of time reversed wave on scatterers. (b) Energy image indicating location of defects. 40

4.9 Simulations results for two scatterers in a dielectric medium. (a) Forward propagating wave from the two sources. (b) Focusing of time reversed wave on scatterers. (c) Energy images indicating defects location. 41

4.10 Simulations results for 1 scatterer in a dielectric medium with permittivity of 4. The number of sensors used is 50. (a) Time reversed waves focus on the scatterer. (b) Energy image indicating maximum energy at defect location. 42

4.11 Simulations results for 2 scatterer in a dielectric medium 2.27λ apart. The number of sensors used is 50. (a) Time reversed waves focus on the scatterers. (b) Energy image indicating maximum energy at defects location. 44

4.12 Simulations results for 2 scatterers in a dielectric medium when noise (SNR=10) is added to the recorded signals. The number of sensors used is 50. (a) Time reversed waves focuses on the 2 scatterers. (b) Energy image indicating maximum energy at defect location. 45

4.13 Simulations results for 2 scatterers in a dielectric medium when noise (SNR=2) is added to the recorded signals. The number of sensors used is 50. (a) Time reversed waves focuses on the 2 scatterers. (b) Energy image indicating maximum energy at defect location. 46

4.14 Simulations results for 2 scatterers in a lossy dielectric medium when σ=0.05. (a) Time reversed waves focuses on the 2 scatterers. (b) Energy image indicating maximum energy at defect location. 47

4.15 Simulations results for 2 scatterers in a lossy dielectric medium when σ=0.1. (a) Time reversed waves focuses on the 2 scatterers. (b) Energy image indicating maximum energy at defect location. 48

4.16 Simulations results for 2 scatterers in a lossy dielectric medium when σ=0.2. (a) Attenuated time reversed waves. (b) Energy image indicating maximum energy at defect location. (c) Energy image indicating maximum energy location. 49

4.17 Simulations results for 2 scatterers 2.27 λ apart in a lossy dielectric medium when σ=0.05. (a) Attenuated time reversed waves. (b) Energy image indicating maximum energy at defect locations. 50

4.18 Attenuation effects from the conductivity (σ=0.08) of the material for 2 scatterers 2.27 λ apart. (a) Comparison between signal from sensor 337 for a lossy dielectric and a dielectric. (b) Signals from sensor 337 for a lossy dielectric. (c) Signals from sensor 337 for a pure dielectric. 51

4.19 Simulations results for 2 scatterers 2.27 λ apart in a lossy dielectric medium when σ=0.08. (a) Attenuated time reversed waves. (b) Energy image indicating maximum energy at defect locations. 52

4.20 Energy image for 2 scatterers 2.27 λ apart in a lossy dielectric medium when σ=0.2 and ε=2.9. 52

4.21 Individual A-scan signals at the receiver when the time delay is modified. 54

4.22 Energy image when signals at all positions were delayed by random quantities. 54

4.23 Individual A-scan signals at the receiver when the time delay is modified. 55

4.24 Energy image when 46 signals were modified. 55

4.25 Individual A-scan signals at the receiver when the time delay and amplitude are modified. 56

4.26 Energy image when 46 signals were modified. 56

4.27 Energy image when time delay is simulated using sensor position error. 57

4.28 Energy image when 11 sensors from a distance of -1.5 to 1.5 m were used in the simulation. 58

4.29 Snapshot from movie showing the place where the waves focus. 58

4.30 Individual A-scan signals at the receivers. 59

4.31 Energy image when 6 sensors from a distance of -1.5 to 1.5 m were used in the simulation. 59

4.32 Snapshot from movie showing the place where the waves focus. 60

4.33 Individual A-scans signals at the receiver. 60

4.34 Individual A-scans signals at the receivers. 61

4.35 Snapshot from movie showing the place where the waves focus. 61

4.36 Energy image when 5 sensors from a distance of -0.6 to 0.6 m were used in the simulation. 62

4.37 Individual A-scan signals at the receivers. 62

4.38 Snapshot from movie showing the place where the waves focus. 63

4.39 Energy image when 6 sensors from a distance of -0.5 to 0.5 m were used in the simulation. 63

4.40 Individual A-scan signals at the receivers. 63

4.41 Snapshot from movie showing the place where the waves focus. 64

4.42 Energy image when 7 sensors from a distance of -0.45 to 0.45 m were used in the simulation. 64

4.43 Energy image when the sensors are 1 m away from the source location. 65

4.44 Energy image when the sensors are 0.7 m away from the source location. 65

4.45 Energy image when the sensors are 0.5 m away from the source location. 65

4.46 Energy image when the sensors are 0.2 m away from the source location. 66

5.1 Experiment Set Up. 68

5.2 Transmitter antenna placed on the arch range. 69

5.3 Receiver antenna on cart. 70

5.4 Experiment performed at a distance of 1.96 m between transmitter and receiver antennas. (a) Picture of experiment when antennas are 1.96 m away. (b) Drawing depicting the distance between the antennas. . 71

5.5 Experiment performed at a distance of 2.90 m between transmitter and receiver antennas. (a) Picture of experiment when antennas are 2.90 m away. (b) Drawing depicting the distance between the antennas. . 72

5.6 Experiment set up when antennas are 1.96m away. 73

5.7 Experiment set up when antennas are 2.90m away. 74

5.8 Plywood panel used to move and avoid shift in the receiver antenna. . 75

5.9 Conducting plate placed between transmitter and receiver antenna. . 76

5.10 Electric field at sensors 1 to 41 for experiment where transmitter antenna is 1.96 m away from receiver antenna. 76

5.11 Electric field at sensors 1 to 41 for experiment where transmitter antenna is 1.96 m away from receiver antenna. 77

5.12 Energy image for experiment performed at a distance of 1.96 m where the energy maximum occurs at (0.053, -0.2740). 77

5.13 Electric field at sensors 1 to 41 for experiment where transmitter antenna is 2.90 m away from receiver antenna. 78

5.14 Energy image for experiment performed at a distance of 2.90 m where the energy maximum occurs at (0.0920, -0.3850). 78

5.15 Experimental signals at a distance of 2.90 m for positions 1 (60 cm), 21 (0 cm), and 41 (-60 cm). 79

5.16 Triangle formed by the measurements taken at the experiment set up. 79

5.17 Triangle formed by the measurements taken at the experiment set up. 80

5.18 Triangle constructed to calculate coordinates of true sensors positions at the experiment set up. 80

5.19 Energy image from simulation of experiment set up. 81

5.20 Experimental signals at a distance of 1.96 m for positions 1 (60 cm), 21 (0 cm), and 41 (-60 cm). 82

5.21 Triangle formed by the measurements taken at the experiment set up. 83

5.22 Triangle formed by the measurements taken at the experiment set up. 83

5.23 Triangle constructed to calculate coordinates of true sensors positions at the experiment set up. 83

5.24 Energy image from simulation of experiment set up. 84

Chapter 1

Introduction

1.1 Introduction to Non-Destructive Evaluation

Detection of defects in critical components and materials without compromising the integrity of the sample is an important area of research in Non-Destructive Testing/Non-Destructive Evaluation (NDT/NDE). NDT/NDE is defined by the American Society of Nondestructive Testing as a test that inspects an object, material or system without damaging the usefulness of the material. Figure 1.1 describes a general NDT/NDE system where the specimen or sample is illuminated with a specific form of energy, the type of energy depends on the nature of the material that is being analyzed, the signals that are produced from the interaction of this energy and material is picked up by the receiving sensor. These signals contain information about the material properties and defects within the material. The signals are processed for material characterization and defect detection purposes.

There are different forms of energy used to illuminate the sample that is inspected and an appropriate method is selected based on the nature of the application. Ultrasound, Eddy currents, Shearography, Magnetic Particle Testing, X-Rays, and Microwaves are some examples of the different techniques and energy sources used in

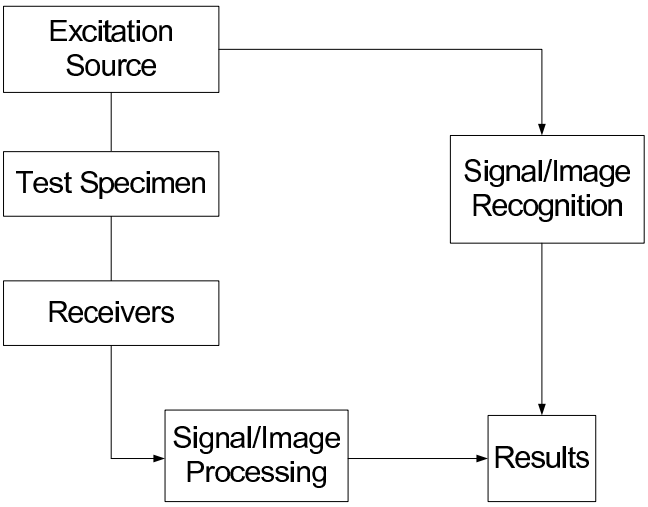

Figure 1.1: General NDT/NDE system

NDT/NDE for the inspection of materials. Ultrasound techniques can determine the thickness of a material and the location of a discontinuity or defect by measuring the time of flight at the reflections from the defects seen as distinct peaks in the signal that is received. The disadvantages of this technique is that it needs a couplant to couple the energy efficiently into the material and secondly, it is difficult for the acoustic signals to penetrate and interact inside porous materials [1]. Eddy current techniques are useful in detecting surface cracks, and near surface cracks, measuring material thickness, coating thickness, and conductivity of samples for material identification and heat damage detection. Eddy current methods are not well suited to inspect dielectric materials because eddy currents can only be induced in conductive materials [1]. Magnetic Particle Testing uses magnetic fields and iron filings to detect defects in ferromagnetic materials. As with eddy current techniques the problem with Magnetic Particle Testing is that it cannot be used to inspect dielectric materials. Radiography is a technique that uses gamma or X-radiation to detect defects. Defects are identified by changes in the image caused by discontinuities/changes in mass density or attenuation constant of materials being inspected. However X-rays present a health hazard, and is not suitable for surface defects. Shearography is an imaging

technique that uses interferometry to obtain real time measurements of changes to a target. It is used to evaluate composites and to detect disbonds, delaminations, and porosity.

Microwave techniques well suited for dielectric materials which allow electromagnetic waves to propagate through and interact with non-conducting structures which is useful for inspection and characterization of composite and dielectric materials [2]. The increasing importance of microwave NDE is largely due to increasing utilization of composite materials in several industries ranging from aviation and automotive to civil infrastructure. Microwaves are also used as an alternate method to inspect new upcoming dielectric and composite materials that are being used in the industry to replace metal. These materials are lighter, stiffer, stronger and electrically insulating and new NDE methods need to be developed for reliably characterizing these materials [3].

1.2 Microwave NDT/NDE principles

Microwave spectrum ranges from 300 MHz to 30 GHz with wavelengths ranges from 1,000 to 10 mm [1]. Microwaves interact better with dielectric and composite materials because they can penetrate deep into these materials. The material-energy interaction is affected by the loss factor associated with dielectric materials and the frequency at which the experiment is conducted [1, 4, 3]. The key advantages of microwave techniques are; it is a non contact method, does not require a couplant as in ultrasound NDE, it is monostatic, and it does not require high power [1].

Microwaves can offer sub-wavelength resolution even though the wavelength is in the centimeter range. Near-field Microwave measurements have shown resolution in the micrometer range for a wavelength of 3cm in free space when monitoring thickness variation in a sample and a resolution of $\lambda/10$ separation between two defects. This

is because lateral resolution in the near field of the different probes that are used is determined by the physical characteristics of the probes. Spatial resolution in the other hand will depend on the type of probe that is selected [3]. The availability of a variety of probes and sensor arrays allows inspection of large areas in an optimal manner.

There are different ways to conduct microwave experiments. Measurements could be done in-contact or non-contact modes. Both of these measurements can be done in transmission or reflection mode. Further, microwaves are also polarized and this characteristic is useful to increase measurement sensitivity to defects of a specific orientation [3].

Microwaves as stated before have many applications in the area of dielectric material characterization. Some of the applications in this area are dielectric mixture constituent determination, porosity evaluation in polymers, moisture measurements, and cure monitoring of resin binders, rubber products and cement-based materials [1]. Microwaves are also useful to determine changes in dielectric sheets thickness and also to detect small defects, thin disbonds, delaminations and the location of these in composites [1]. Defects on metals surfaces, fatigue crack detection and sizing under paint in metals, corrosion under paint, and corrosion precursor pitting impact damage on carbon based composite are some examples of the inspection capabilities of microwaves [1]. Microwaves have also been used for biological applications [1].

Cement-based materials are commonly inspected using microwaves NDT/NDE. These materials are used extensively in the construction industry and for this reason their inspection is crucial for security and quality control reasons. In [5] the reflection and transmission properties of cement-based materials were analyzed. To determine properties of this material at the first stages of the hydration process and that in order to perform long time monitoring of hardened cement-based materials transmission measurements were used. They also found that because of the porosity of the cement

materials, higher transmission coefficient measurements correspond to initial high water content in the material. The authors found that the amplitude of reflection and transmission coefficients was related to the permittivity of the material. It was shown in [5] that the reflection coefficient depends on the real part of the permittivity and that the transmission coefficient depends on the imaginary part of the permittivity.

Microwave measurements of reflection and transmission coefficients can be done in the near-field and far-field. Arunachalam *et al.* [6] presents a feasibility study about far-field microwave frequency domain reflection measurements to produce images of cement-based materials. They produced good images of planar mortar, concrete, and steal bar inside concrete samples using simple post-processing techniques. Boise *et al.* [7] presents the use of microwave near field reflection measurements to evaluate the material content of concrete. Where an open-ended rectangular waveguide probes measure the reflection coefficient of different concrete samples with different material constituents to determine the compressive strength of concrete. The paper concludes that the reflection measurements obtained from the samples follow different statistical distributions. At 10 GHz the specimens that were measured followed a Gaussian distribution and at this frequency there was also a correlation with concrete coarse aggregate to cement ratio. At 3 GHz the results followed a uniform distribution and the mean of the reflection coefficient at this frequency had a correlation with water to cement ratio [7].

Carbon fiber reinforced polymer (CFRP) is a composite material that is used to reinforce structures such as bridges. This materials need to be inspected to determine if they become disbonded from the structure to which they were attached. In order to inspect these materials a dual-polarized near-field microwave reflectometer was used in [8]. This technique takes advantage of the anisotropy presented in unidirectional CFRP laminates. Microwaves reflect of the CFRP when the polarization of the electric field is normal to the fiber dimensions and they penetrate the material

when the polarization is parallel to the fiber dimensions [8]. The authors use these properties to generate images of the CFRP using perpendicular polarization to detect disbonds in the material and parallel polarization to remove influences due to surface roughness, and standoff distance change from perpendicular polarization [8]. This technique provided images in which disbonds locations and sizes could be seen.

Layered composite materials are also evaluated with NDT/NDE techniques with good results. Zoughi *et al.* [9, 10] developed techniques to detect the presence of corrosion under thin layers of paint and primer, which are considered dielectrics. It was found in this research that the phase of the reflection coefficient at high frequencies is useful to detect corrosion. In this research open-ended rectangular waveguides are used to achieve detection of corrosion under layers of paint and primer.

Delamination cracks in thermal barrier coatings (TBCs) are also a problem in the aerospace industry. TBCs cover the components of gas turbines to avoid overheating of these parts [11]. The authors found that at around 55 to 65 GHz, the amplitude and phase of the transmission coefficient contain information about location and characterization of the defects.

1.3 Forward and Inverse Problem

In an inverse problem, the transfer function of a system is estimated. The transfer function describes the system characteristics. By analyzing the output and input of the system, the transfer function can be found; this is the central principle of the inverse problem[12].

In NDT/NDE inverse problem, an energy source is used to illuminate a sample and the response signal is analyzed to detect and characterize defects in the sample [13]. Figure 1.2 illustrate an inverse problem system. The input and output are known but the system parameters are unknown. Usually the input is an excitation

signal from a transmitting transducer and the output is the response of the system to the excitation signal. Using these two known signals a system can be identified [14]. In NDT/NDE the structure of the object under test is known but internal parameters such as defects, their location, and shape characteristics need to be estimated.

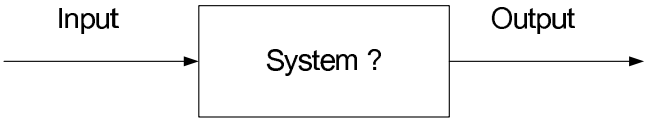

Figure 1.2: Inverse problem description

The inverse problem is in general ill-posed. An ill-posed problem is one where the solutions are non unique and non continous [12]. The fact that the solutions are unstable and non unique is a problem because the information contained in the output signal corresponds to more than one defect profile [15].

Methods to overcome these issues with inverse problems solutions are a major area of interest in NDT/NDE. One of the techniques used to solve the inverse problem is the iterative approach. The iterative approach involves the solution of the forward problem using forward models, which are discussed in section 1.4.

Unlike inverse problems, forward problems are well-posed. In contrast to an ill-posed problem, well-posed problems are stable, which means that the solution depends continuously on the given input data. Well-posed problems generate accurate and unique solutions. There are two types of forward problems: direct problem and signal detection problem, illustrated in figure 1.3. Figure 1.3 (a) describes a direct problem. In a direct problem the output of the system is found because the input and the transfer function of the system are known. Figure 1.3 (b) describes a signal detection problem. In a signal detection problem the input is found when the output and the system are known [14].

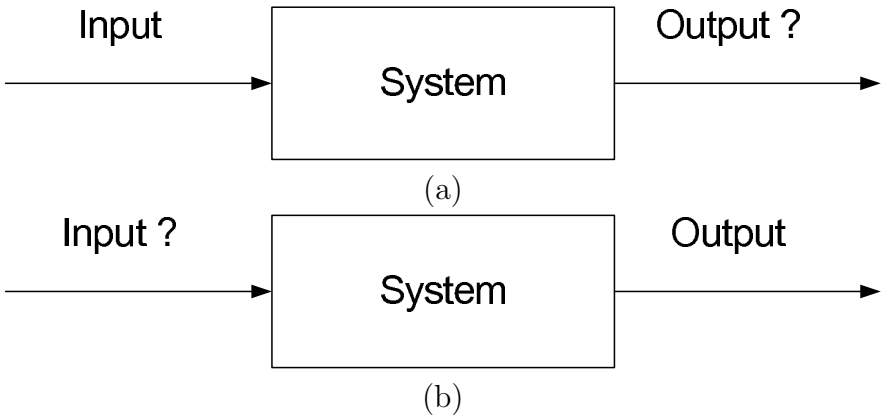

Figure 1.3: Forward problem description. (a) Forward problem classified as the direct problem. (b) Forward problem classified as the signal detection problem.

1.4 Model-Based Approach

Iterative approaches, that involve the solution of the forward problem, are used to solve the inverse problem. Figure 1.4 describes the overall model-based process. The algorithm starts with an estimate of the system and solves the forward problem to obtain the output signal. The error between the measured signals and the simulated output signals is minimized iteratively by updating the defect profile. If the error calculated is above a given threshold, the defect parameters are updated and the process is repeated until the error is below the threshold. When the error is below the threshold, the defect parameter is the desired solution [16]. The iterative approach requires an accurate forward model. Forward models are numerical models based on integral and differential equations.

There are different numerical methods used to solve the inverse problem. Finite-difference method (FDM), boundary element method (BEM), and the well known finite-element method (FEM) are examples of numerical methods used to create computational models. However, use of a computational numerical model in an iterative framework results in exorbitant computational resources. This thesis presents a non-iterative model-based method for solving the inverse problem.

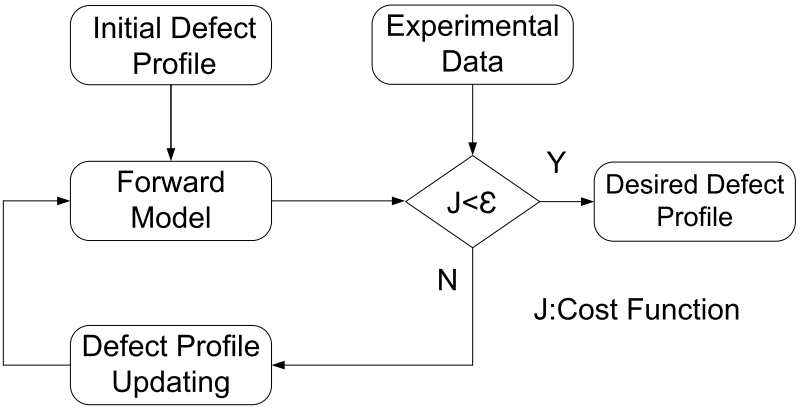

Figure 1.4: Iterative process to solve the inverse problem

1.5 Time Reversal approach for inverse problems

Time reversal focusing is based on the fact that when a wave solution is reversed in time and back propagated it comes to focus at the source. In acoustics the propagation equation for a pressure field in a lossless medium is given by equation 1.1

$$\vec{\nabla} \bullet \left(\frac{\vec{\nabla} p}{\rho} \right) - \frac{1}{\rho c^2} \frac{\partial^2 p}{\partial t^2} = 0 \tag{1.1}$$

where $p(r,t)$ is the pressure field $\rho(r)$ is the density and $c(r)$ is the sound velocity. Because of invariance under Time Reversal both $p(r,t)$ and $p(r,-t)$ are solutions of the propagation equation. This property can be exploited to use wave measurements for imaging sources or scatterers /defects in a test specimen.

Time Reversal experiments in ultrasound are usually performed using a time reversal mirror that is made of an array of transmit-receive transducers. In [17] experiments were performed to detect kidney stones in aberrating media. These experiments proved to be successful in detecting the stones and focusing on a small portion of them through aberrating media. Time Reversal had also been used to detect flaws in thin plates by increasing the signal to noise ratio [18]. It is very difficult to detect flaws using Lamb waves but time reversal, because of the invariance property, reduces the

dispersion of Lamb waves allowing the flaws on thin plates to be detected.

Time reversal of microwave fields has also been studied. Kosmas et al. have developed a finite difference time domain (FDTD) time reversal as a matched filter approach for microwave breast cancer detection [19, 20]. Experiments done in microwave time reversal are presented in [20]. This thesis presents a feasibility study, using computational model, of applying principles of time reversal to microwave NDE data for solving the inverse problem of defect detection in dielectric materials.

1.6 Contributions

The major contribution of this work is development of an FDTD forward model and time reversal techniques to solve the inverse problem of defect detection in Microwave NDE. The main advantage combining these two techniques, time reversal and forward models, is that an iterative solution to the inverse problem is not needed. Usually iterative methods, where the minimization of an error is required, can encounter convergence problems, are time consuming and computationally expensive.

The dissertation consists of the following chapters. Chapter 2 describes the finite difference time domain formulation and boundary conditions applied. Time reversal theory is discussed in Chapter 3. Validation of time reversal analysis is discussed in Chapter 4. The application of time reversal techniques for defect imaging and the results obtained with different defects and in the presence of noise are also presented in Chapter 4. Concluding remarks are given in Chapter 5. Future work is presented in Chapter 6.

Chapter 2

Forward Model

2.1 Introduction

In this thesis a numerical model for solving the forward problem of microwave propagation through a material is developed. A brief description of the numerical model based on finite difference time domian (FDTD) method is presented in this chapter. In FDTD, the time-dependent Maxwell's equations are discretized using centered two point finite differences to approximate the spatial and time derivatives. The formulation uses absorbing boundary conditions. Simulation results for several NDE geometries are presented in Chapter 4.

2.2 Maxwell Equations

The underlying equation governing NDE inspection can be derived from Maxwell's equations. The Maxwell-Ampere's and Maxwell-Faraday's laws for time varying electromagnetic fields are:

$$\frac{\partial \vec{D}}{\partial t} = \nabla \times \vec{H} - \vec{J} \tag{2.1}$$

$$\frac{\partial \vec{B}}{\partial t} = -\nabla \times \vec{E} \tag{2.2}$$

The divergence equations are:

$$\nabla \cdot \vec{D} = \rho \tag{2.3}$$

$$\nabla \cdot \vec{B} = 0 \tag{2.4}$$

In linear, isotropic, time-invariant, nondispersive media, the fluxes, $\vec{D}$ and $\vec{B}$, and the fields strengths, $\vec{E}$ and $\vec{H}$, are related by material parameters.

$$\vec{D} = \varepsilon \vec{E} \tag{2.5}$$

$$\vec{B} = \mu \vec{H} \tag{2.6}$$

Substituting equation (2.5) in equation (2.1)

$$\varepsilon \frac{\partial \vec{E}}{\partial t} = \nabla \times \vec{H} - \vec{J} \tag{2.7}$$

After substituting equation (2.6) in equation (2.2)

$$\mu \frac{\partial \vec{H}}{\partial t} = -\nabla \times \vec{E} \tag{2.8}$$

where the variables are:

$\vec{E}$: Electric Field Intensity (V/m)

$\vec{H}$: Magnetic Field Intensity (A/m)

$\vec{D}$: Electric Flux Density (C/m^2)

$\vec{B}$: Magnetic Flux Density (T)

$\vec{J}$: Electric Current Density (A/m^3)

ρ: Electric Charge Density (C/m^3)

ε: Permittivity

μ: Permeability

In free space and a charge free environment, Maxwell's equations are:

$$\nabla \cdot \vec{E} = 0 \tag{2.9}$$

$$\nabla \cdot \vec{B} = 0 \tag{2.10}$$

$$\frac{\partial \vec{B}}{\partial t} = -\nabla \times \vec{E} \tag{2.11}$$

$$\mu\varepsilon \frac{\partial \vec{E}}{\partial t} = \nabla \times \vec{B} \tag{2.12}$$

By applying different vector identities to these equations, the wave equation for source-free uniform lossless media is obtained. The first step is to find the curl of equation (2.2).

$$\nabla \times \left(\nabla \times \vec{E} \right) = \nabla \times \left(-\frac{\partial \vec{B}}{\partial t} \right) \tag{2.13}$$

The curl of the curl is given by:

$$\nabla \times \left(\nabla \times \vec{E} \right) = \nabla \left(\nabla \cdot \vec{E} \right) - \nabla^2 \vec{E} \tag{2.14}$$

Producing the equation (2.13)

$$\nabla \left(\nabla \cdot \vec{E} \right) - \nabla^2 \vec{E} = -\frac{\partial}{\partial t} \left(\nabla \times \vec{B} \right) \tag{2.15}$$

Substituting equations (2.9) and (2.12) into equation (2.15) gives the electromag-

netic wave equation in terms of the electric field

$$\nabla^2 \vec{E} = \mu\varepsilon \frac{\partial^2}{\partial t^2} \vec{E} \tag{2.16}$$

$$\nabla^2 \vec{E} = \frac{1}{c^2} \frac{\partial^2}{\partial t^2} \vec{E} \tag{2.17}$$

where c is the wave propagation speed given by $c = \frac{1}{\sqrt{\mu\varepsilon}}$ and $\vec{E}$ is the electric field.

Following the same steps the electromagnetic wave equation in terms of the magnetic field can be found. The first step is to find the curl of equation (2.12).

$$\nabla \times \left(\nabla \times \vec{B} \right) = \nabla \times \left(\frac{1}{c^2} \frac{\partial \vec{E}}{\partial t} \right) \tag{2.18}$$

After finding the curl of equation (2.12) and using the definition of the curl of the curl given in (2.14)

$$\nabla \left(\nabla \cdot \vec{B} \right) - \nabla^2 \vec{B} = \frac{1}{c^2} \frac{\partial}{\partial t} \left(\nabla \times \vec{E} \right) \tag{2.19}$$

Substituting equation (2.4) and equation (2.2) into equation (2.19) gives

$$-\nabla^2 \vec{B} = \frac{1}{c^2} \frac{\partial}{\partial t} \left(\frac{-\partial \vec{B}}{\partial t} \right) \tag{2.20}$$

Rearranging the terms in equation (2.20) produces the electromagnetic wave equation in terms of the magnetic field

$$\left(\nabla^2 - \frac{1}{c^2} \frac{\partial^2}{\partial t^2} \right) \overrightarrow{B} = 0 \tag{2.21}$$

where c is the speed of light, and $\vec{B}$ is the magnetic flux density.

The FDTD algorithm is based on the solution of Ampere's and Faraday's laws

using centered two point finite differences to approximate the spatial and time derivatives in these equations. The derivatives are replaced by

$$\left.\frac{df}{dz}\right|_{z=z_0} = \frac{f(z_0+\Delta z/2) - f(z_0-\Delta z/2)}{\Delta z} \tag{2.22}$$

After the derivatives in the Ampere's and Faraday's laws are approximated by centered two point finite differences, the equations to solve the magnetic and electric fields are expressed in terms of the past magnetic and electric fields values. The magnetic and electric fields are then solved one time step into the future and the process is repeated until all the fields are calculated over the desired duration.

2.3 FDTD Spatial and Time Discretization

Transverse magnetic (TM) polarization was used for these simulations. This means that there is no magnetic field in the z direction. For this case Maxwell's curl equations reduce to

$$E_x = E_y = 0, H_z = 0 \tag{2.23}$$

$$\varepsilon\frac{\partial E_z}{\partial t} = \frac{\partial H_y}{\partial x} - \frac{\partial H_x}{\partial y} \tag{2.24}$$

$$\mu\frac{\partial H_x}{\partial t} = -\frac{\partial E_z}{\partial y}, \mu\frac{\partial H_y}{\partial t} = -\frac{\partial E_z}{\partial x} \tag{2.25}$$

The spatial FDTD discretization is achieved by approximating the spatial derivatives by two-point centered differences. For example the spatial FDTD approximation to equation (2.25) is given by

$$\begin{aligned} &\mu\frac{\partial H_x}{\partial t} = -\frac{\partial E_z}{\partial y} \\ &-\mu\frac{H_x[i,j+\frac{1}{2}] - H_x[i,j+\frac{1}{2}]}{\Delta t} = \frac{E_z[i,j+1] - E_z[i,j]}{\Delta y} \end{aligned} \tag{2.26}$$

After the two-point centered difference is applied to the spatial derivatives it could be noticed that the electrical field nodes are located at integer spatial steps and that the magnetic field nodes are located at half integer spatial steps. The location of the electric and magnetic fields in the two different grids is shown in Figure 2.1.

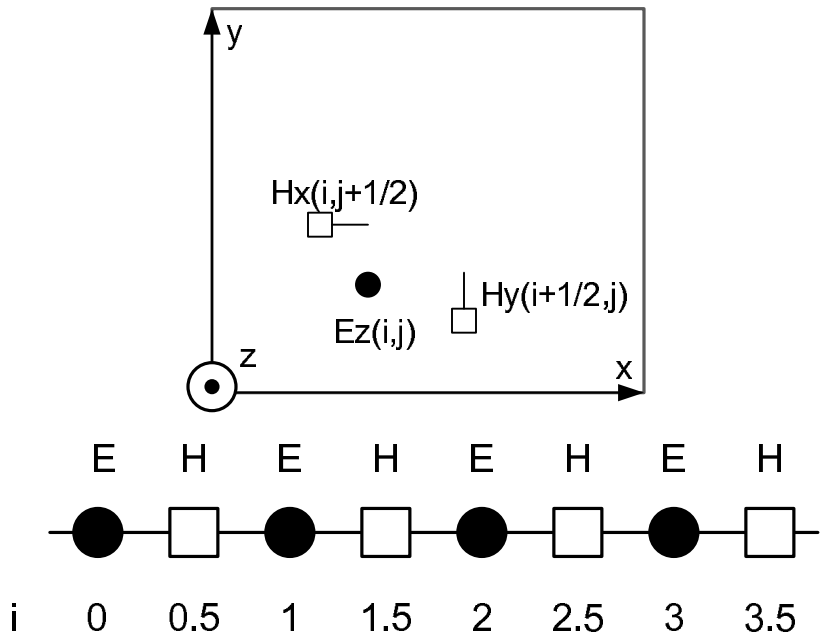

Figure 2.1: Spatial Grid for the FDTD algorithm.

Centered finite-difference approximations are also used to discretize the fields in time domain. After the approximations are made the electric field exists at integer time steps and the magnetic fields are offset half time step from the electric fields. The fields are advanced in time using the same fields but at a different instant in time, the past instant in time in the grid, and also using the opposite field type at an intermediate instant in time. The solution of the fields depends only on past field values. Figure 2.2 shows the time discretization scheme.

After replacing the spatial and time derivatives in Faraday's and Ampere's equations using centered finite-differences, the equations for the magnetic and electric

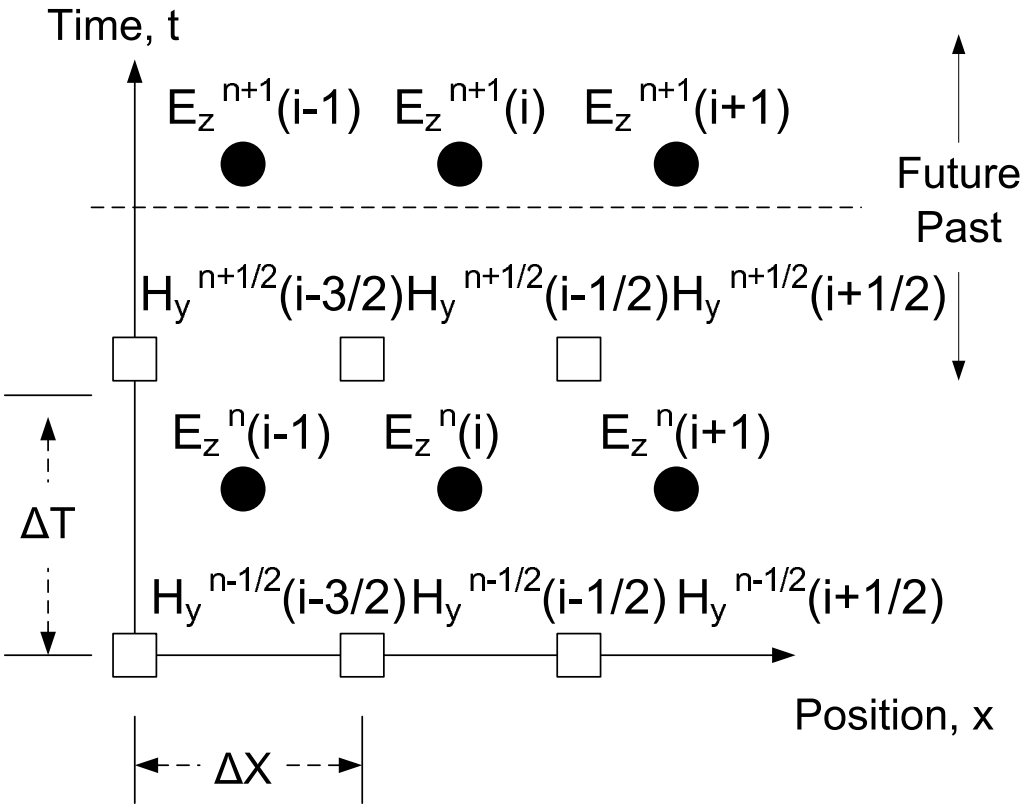

Figure 2.2: FDTD Time Discretization Scheme.

fields used in the FDTD algorithm for TM polarization are:

$$H_x{}^{n+\frac{1}{2}}\left[i,j+\frac{1}{2}\right] = \frac{1-\frac{\sigma_i\Delta_t}{2\mu}}{1+\frac{\sigma_i\Delta_t}{2\mu}} H_x{}^{n-\frac{1}{2}}\left[i,j+\frac{1}{2}\right] - \frac{1}{1+\frac{\sigma_i\Delta_t}{2\mu}}\frac{\Delta_t}{\mu\Delta y}\left(E_z{}^{n}\left[i,j+1\right]-E_z{}^{n}\left[i,j\right]\right) \tag{2.27}$$

$$H_y{}^{n+\frac{1}{2}}\left[i+\frac{1}{2},j\right] = \frac{1-\frac{\sigma_i\Delta_t}{2\mu}}{1+\frac{\sigma_i\Delta_t}{2\mu}} H_x{}^{n-\frac{1}{2}}\left[i+\frac{1}{2},j\right] + \frac{1}{1+\frac{\sigma_i\Delta_t}{2\mu}}\frac{\Delta_t}{\mu\Delta x}\left(E_z{}^{n}\left[i+1,j\right]-E_z{}^{n}\left[i,j\right]\right) \tag{2.28}$$

$$
\begin{aligned}
{E_z}^{n+1}[i,j] = {} & \frac{1-\frac{\sigma\Delta_t}{2\varepsilon}}{1+\frac{\sigma\Delta_t}{2\varepsilon}} {E_z}^{n}[i,j] \\
& + \frac{1}{1+\frac{\sigma\Delta_t}{2\varepsilon}} \left(\begin{array}{l} \frac{\Delta_t}{\varepsilon\Delta x}\left\{ {H_y}^{n+\frac{1}{2}}\left[i+\frac{1}{2},j\right] - {H_y}^{n+\frac{1}{2}}\left[i-\frac{1}{2},j\right] \right\} \\ -\frac{\Delta_t}{\varepsilon\Delta y}\left\{ {H_x}^{n+\frac{1}{2}}\left[i,j+\frac{1}{2}\right] - {H_x}^{n+\frac{1}{2}}\left[i,j-\frac{1}{2}\right] \right\} \end{array} \right)
\end{aligned}
\tag{2.29}
$$

Stability conditions have to be met in order to obtain accurate solutions for the equations that are approximated using finite differences. It is necessary that the field solutions do not change significantly from one point in the grid to the other. To achieve this the grid steps must be the same in each direction, $\Delta x = \Delta y$ [21, 22]. For the two dimensional FDTD code the stability condition is given by $c\Delta t \leq \frac{\Delta x}{\sqrt{2}}$.

2.4 Absorbing Boundary Conditions

FDTD is used to solve time-domain electromagnetic-field equations in an unbounded space. In order to limit the domain in which the field is computed, a mesh of limited size and boundary conditions are used. Absorbing boundary conditions are used on the outer surface of the mesh to accurately model the unbounded surroundings in the computational domain. There are different kinds of absorbing boundary conditions that are used in FDTD simulations to avoid fields reflections. The one selected for these simulations falls into the One-way wave equations, specifically the ones developed by Mur [23]. One-way wave equations consist of a partial differential equation that supports wave propagation in certain directions only. For example, if the computational domain is defined in the area of $x > 0$ then FDTD equations already defined are used but at the boundaries of the computational domain, such as x=0,

one-way wave equations are used. In this case absorbing boundary conditions are needed for the H-field components that are tangential to the boundary of interest. For the outgoing wave the first order boundary condition is given by

$$\left(\partial_x - {c_0}^{-1}(1-(c_0 s_y)^2-(c_0 s_z)^2)^{\frac{1}{2}}\partial_t\right) W_{x=0} = 0 \tag{2.30}$$

where s_y, s_z are the inverse velocity components, c is the speed of light and W is the H_x or H_y for TM to z. This equation solves for W on the outer surface, which is consistent with an outgoing wave. An approximation of this equation is made in order to account for the fact that the angle of incidence of the wave approaching x=0 is unknown. After the approximation is made the finite difference approximation equations used to implement absorbing boundary conditions in the FDTD code are:

$${H_y}^{n+\frac{1}{2}}[i,0] = {H_y}^{n-\frac{1}{2}}[i,1] + \frac{c_0\Delta_t - \Delta_x}{c_0\Delta_t + \Delta_x}\left({H_y}^{n+\frac{1}{2}}[i,1] - {H_y}^{n-\frac{1}{2}}[i,0]\right) \tag{2.31}$$

$${H_x}^{n+\frac{1}{2}}[0,j] = {H_x}^{n-\frac{1}{2}}[1,j] + \frac{c_0\Delta_t - \Delta_x}{c_0\Delta_t + \Delta_x}\left({H_x}^{n+\frac{1}{2}}[1,j] - {H_x}^{n-\frac{1}{2}}[0,j]\right) \tag{2.32}$$

2.5 Source

There are different kinds of sources. Additive source is the one used in these simulations. The additive source is introduced in the FDTD algorithm through Ampere's law, which is one of Maxwell's equations that contain the current density term. The current density $\vec{J}$ has two different meanings, the conduction current due to the flow of charge in a material due to an electric field or the current of a source. For this case $\vec{J}$ represents the current generated by a source and in this case is defined to be a gaussian or quasi-gaussian pulse. The source could be applied to one or more than

one node.

$$\frac{\partial \vec{E}}{\partial t} = \frac{1}{\varepsilon}\nabla \times \vec{H} - \frac{1}{\varepsilon}\vec{J} \tag{2.33}$$

The equation that is used in the FDTD algorithm after the centered finite-difference approximations are applied is

$$\begin{aligned} {E_z}^{n+1}[i,j] = {} & \frac{1-\frac{\sigma\Delta_t}{2\varepsilon}}{1+\frac{\sigma\Delta_t}{2\varepsilon}} {E_z}^{n}[i,j] \\ & + \frac{1}{1+\frac{\sigma\Delta_t}{2\varepsilon}} \left(\begin{array}{c} \frac{\Delta_t}{\varepsilon\Delta_x}\left\{ {H_y}^{n+\frac{1}{2}}\left[i+\frac{1}{2},j\right] - {H_y}^{n+\frac{1}{2}}\left[i-\frac{1}{2},j\right] \right\} \\ -\frac{\Delta_t}{\varepsilon\Delta_y}\left\{ {H_x}^{n+\frac{1}{2}}\left[i,j+\frac{1}{2}\right] - {H_x}^{n+\frac{1}{2}}\left[i,j-\frac{1}{2}\right] \right\} \end{array} \right) \\ & - \frac{\Delta t}{\varepsilon} {J_z}^{n+\frac{1}{2}}[i,j] \end{aligned} \tag{2.34}$$

This chapter presented the underlying governing equations for microwave NDE and formulation of the FDTD method. The differential equations that describe Ampere's and Faraday's laws are approximated using two-point centered differences. And absorbing boundary conditions are imposed. The source configurations used in the Forward Model were also presented. The next chapter presents how the Forward Model is used to solve the inverse problem. The Forward Model is validated in Chapter 4.

Chapter 3

Inverse Problem Solution Using Time Reversal Techniques

3.1 Introduction to Inverse Problems in NDE/NDT

Defect locations or profiles in NDE/NDT, requires the solution of inverse problems using information in the measured signal, that is provided by experimental or model based data [24]. Inverse problems are mathematically ill posed because the uniqueness and stability of the solution can not be guaranteed [25]. There are different proposed techniques to solve the inverse problem. Some of the techniques used to solve inverse problems are calibration techniques, direct, and indirect approaches [24].

3.1.1 Calibration Techniques

Calibration techniques involve the creation of calibration curves that are used to obtain defect information. Features in experimental data are acquired for different geometrical parameters of known defects. The geometric parameters include defect characteristics such as width, depth, length, angle of inclination to the surface, and the distance of the defect to the surface. In order to obtain the calibration curves

the defect characteristics are changed one at changes in signal features vs. defect characteristic being changed are plotted. This method can only be used if the defects shapes are known beforehand. This means that if the defect shapes are different from the ones used to create the calibration curves the method is not useful to solve the inverse problem [26].

3.1.2 Direct Methods

Electromagnetic NDE problems assuming linear and isotropic conditions can be modeled by equation (3.1):

$$(\nabla + k^2)h(\vec{x}) = f(\vec{x}) \tag{3.1}$$

where $f(\vec{x})$ is the source in terms of current densities or charges, and h represents the electric or magnetic field that is used to find the defects in the material. Equation (3.1) represents the wave equation when the wavenumber is $k^2 > 0$. Assuming linearity, equation (3.1) can be expressed in integral form by equation (3.2)

$$h(\vec{x}) = \int_v G(\vec{x}, \vec{x}')f(\vec{x}')dx, \tag{3.2}$$

where $G(\vec{x}, \vec{x}')$ is the Green's function. A discrete-space version of equation (3.2) is given by:

$$\{h\} = \{G\}\{f\}. \tag{3.3}$$

In direct methods, for solving the inverse problem, the matrix presented in equation (3.3) is solved for f, where f represents the source or defects. The disadvantage of this method is that produces an unreliable solution due to ill conditioning of matrix G [26]. A small error or change in G causes a large error or change in f due to the high condition number of matrix G. The direct approach makes the solution to the inverse problem for defect detection unreliable.

3.1.3 Indirect Inversion

There are two types of indirect methods used to solve the inverse problem: phenomenological/model-based and algorithm/signal classification based. Phenomenological/model based approaches are based on the underlying physics of the NDE method. A forward model simulating the physics is used in an iterative processes where the forward problem is solved in each iteration. The process starts assuming an initial defect profile and a signal, corresponding to this defect characteristic, is generated using a forward model. After this signal is generated using the model, it is compared to an experimental signal. If the error between this two signals does not meet an established threshold, the process is repeated assuming a different defect profile, which is adjusted using the error information [24]. This process is illustrated in figure 3.1. It is important to choose the appropriate forward model in order to obtain reliable results. A major drawback of this approach is that solving a numerical model in each iteration makes it computationally demanding and the method can take very long times.

In the non-phenomenological approach, the inverse problem is formulated as a defect classification problem. The measured signal is classified onto a set of different known types of sources or defect signals. Algorithmic/signal classification-based approach require a training database consisting of a collection of defect signals from a variety of defects. This data bank is used to train the algorithm to detect and identify different classes of defects in materials using features in the experimental data [26].

The method presented in this work, to solve the inverse problem, is model-based. Model-based methods depend on the interaction of the field, which is illuminating the sample, with the different flaws in the material. Model-based methods that are used in an iterative manner are time consuming and computationally expensive. The advantage of the model-based method, presented in this work, to solve the inverse

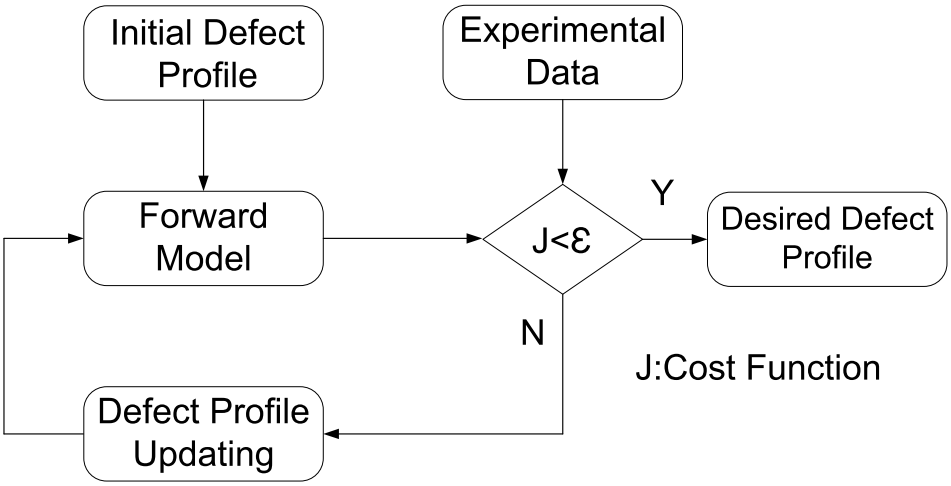

Figure 3.1: Model based iterative method to solve the inverse problem.

problem is that is not an iterative method.

3.2 Previous Research: Time Reversal Technique used in Ultrasound and Microwaves

Extensive work has been done in time reversal, specifically in the ultrasound field. Basic principles and the validation of the technique with experimental results are presented in [27, 17]. The signals created after time reversal are focused signals that have characteristics of the defect and the medium in which the wave propagates. Time reversal, using ultrasound, is used to find defects in materials because it is able to reduce speckle noise due to the fact that the time reversed signal that comes from a defect has specific properties of the defect [28]. After the signals are processed, using normalized correlation coefficient and deviation histogram techniques, the defect can be detected and distinguished from the speckle noise zone.

A variety of materials have been inspected using time reversal techniques. An important application of this technique is inspection of titanium. Titanium is a noisy medium, therefore strong ultrasonic speckle noise is induced by the polycrystalline

microstructure. It also contains hard-α defects. These defects are hard to detect because of the low reflectivity caused by acoustic impedance mismatch, furthermore these defects have irregular and unknowns shapes. Time reversal techniques overcome these difficulties because it is a process that is matched to the defect shape and to the propagation medium. It also compensates for distortions due to the propagation through inhomogeneous media.

Chakroun *et al.* [29] experiments were conducted with titanium using iterative time reversal which showed that defect and speckle noise signals had different characteristics. They developed a new noise reduction technique using deviation histogram which allows distinguishing between noise and defect signal. In [30], time reversal technique is optimized to avoid false identification of defects, to reduce noise amplitude in the signal, and it is used to detect defects in titanium billets. In order to optimize the technique two new refocusing processes were developed, iterative matched filter and iterative coherent summation. The matched filter technique allows the detection of defects of the size 0.6mm at a 140mm depth in a titanium billet of 250mm.

Defects in duralumin alloy have also been detected using time reversal techniques. In [31] a complex geometry of this material with a 2 mm flat bottom hole defect was studied. The defect in the material was easily detected using time reversal techniques. Study of time reversal of ultrasound fields, has demonstrated the capability of the technique for detecting small defects in complex geometries and for distinguishing between defects and speckle noise.

Time reversal is also used to detect defects in thin plates using lamb waves. Lamb waves are very useful to inspect plates because of their guided characteristic. Their disadvantage is that they are very dispersive and this characteristic limits their use for non destructive evaluation testing. Time reversal allows the use of lamb waves for defect detection because it compensates for the disadvantage of lamb waves. The

effect of time reversal in the detection of flaws using lamb waves is validated with experimental data in [18].

In [32, 33] elastic waves are propagated and they interact with a circular cylinder tube. The fields are recorded, time reversed, and propagated in a FDTD model in order to find defects in this circular cylinder tube. This work presents the simulation results with experimental data. The results show that the signals that are propagated in the FDTD model focus on the location where the actual circular cylinder tube had the defect. FDTD and time reversal had also been used in microwave breast cancer detection. In [19] a feasibility study is performed using FDTD as the model used to detect breast cancer. The paper presents simulation results that show the time reversed signals focusing on a tumor inside a breast model.

3.3 Previous Research: Time Reversal Used to Solve the Inverse Problem

Time reversal has been used to solve the inverse problem. The work presented in [34] proposes a time domain topological gradient as an inverse method for ultrasound. The topological gradient is a function of the forward and adjoint problems. The adjoint problem mathematical solution is based on the physical time reversal operation. Applying time reversal techniques to the solve the adjoint problem prevent the method to fall into a local minimum, which will eventually lead to a non-physical solution. This is due to refocusing properties that times reversal provides.

In [35] the information of the scattered field was used to characterize a spatially extended scatterer. In the presence of a spatially extended scatterer there are two types of waves that are generated after the waves interact with the defect. The first reflected wave corresponds to the target geometry and the rest of the reflected waves correspond to circumferential and volume waves that propagate around or inside

the scatterer. The inverse problem for this case, consists in the characterization of circumferential waves. Circumferential waves are related to the normal modes of vibration of the cylinder and these waves also represent its acoustical mark.

3.4 Proposed Approach to Solve the Inverse Problem in NDE/NDT: Time Reversal Technique using an FDTD Model

The propagation of electromagnetic waves through a material or free space is given by equation (3.4), a second order partial derivative equation, where $\vec{E}$ is the electric field and c is the speed of light. Because of invariance under Time Reversal, both $E(r,t)$ and $E(r,-t)$ are solutions to the wave equation presented in 3.4. Invariance is a characteristic of the wave equation that allows the system to be unchanged under certain transformations, in this case a time transformation. Time reversal focusing is based on the fact that when a wave solution is reversed in time and back propagated it comes to focus at the source. Time reversal principle is only valid for a lossless propagation medium. When the propagation medium contains frequency-dependant attenuation, invariance and time reversal properties are invalid due to the fact that the wave equation contains an odd order time derivative operator [27].

$$\left(\nabla^2 - \frac{1}{c^2}\frac{\partial^2}{\partial t^2}\right)\overrightarrow{E} = 0 \tag{3.4}$$

3.4.1 Mathematical Background

In time reversal acoustic experiments the receivers, which are transducers, are known as time reversal mirrors (TRMs). In microwave experiments, the TRM is a single or an array of antennas. The antenna or the array of antennas is placed in the far field

of the source [36]. The first step in a time reversal experiment is to illuminate the sample using a time domain pulse emitted from the transmitter antenna at position $\vec{r}_s$. The fields incident on the target, which is located at position $\vec{r}$, are [37, 38]:

$$E^{inc}(\vec{r},t) = p(t) * G(\vec{r},\vec{r}_s,t) = \int p(\tau)G(\vec{r},\vec{r}_s,t-\tau)d\tau \tag{3.5}$$

where $p(t)$ is the time domain pulse and $G(\vec{r},\vec{r}_s,t)$ represents the Green's function of the background medium, which is the solution to equation (3.6).

$$\nabla \times \nabla \times \vec{G} - k^2\vec{G} = \vec{I}\delta \tag{3.6}$$

The incident field in the frequency domain is given by equation (3.7),

$$E^{inc}(\vec{r},\omega) = P(\omega)G(\vec{r},\vec{r}_s,\omega) \tag{3.7}$$

where $P(\omega)$ is the spectrum of the pulse.

The second step consists on recording the scattered field on the receiving antenna or array. The scatter field measured at receiver i is given by equation (3.8),

$$E^{scatter}(\vec{r}_i,\omega) = {k_b}^2(\omega) \int E(\vec{r},\omega)G(\vec{r}_i,\vec{r},\omega)O(\vec{r},\omega)d\vec{r} \tag{3.8}$$

where $\vec{r}_i$ is the location of the ith receiver, $E(\vec{r},\omega)$ is the total field resulting from the incident field. The total field, inside the scatterer, is a function of $O(\vec{r},\omega)$, which makes equation (3.8) non-linear [39]. The scattered field can also be represented using the Born approximation in order to linearize equation (3.8). The Born approximation states that the effect of the incident field on the targets is small and a first approximation of the total field, $E(\vec{r},\omega)$, in equation (3.8) can be set equal to the incident field [28, 40]. The resulting equation is given by:

$$E^{scatter}(\vec{r}_i,\omega) = {k_b}^2(\omega)\int E^{inc}(\vec{r},\omega)G(\vec{r}_i,\vec{r},\omega)O(\vec{r},\omega)d\vec{r} \tag{3.9}$$

$O(\vec{r},\omega)$ is the object function to be imaged and is given by equation (3.10),

$$O(\vec{r},\omega) = \frac{k^2(\vec{r},\omega)}{{k_b}^2(\vec{r},\omega)} - 1 \tag{3.10}$$

where the wavenumbers of the total medium, including background and targets, and background medium alone are k^2,${k^2}_b$, respectively.

The third step in the time reversal process is to time reverse the scattered fields that were recorded by the receiver antennas. In order to achieve time reversal the medium has to be reciprocal and non-absorbing. In the frequency domain time reversal is performed by phase conjugating the received field at each receiver position. After the fields are time reversed, they are propagated from the receiver location.

3.4.2 Time Reversal Focusing

Time reversal focusing is similar to matched-filter techniques used in signal processing. A matched filter is an ideal linear filter which maximizes the signal to noise ration (SNR) of the filtered signal. For example, in an acoustic experiment, a pulse $\delta(t)$, at position $\vec{r}_s$, is propagated. The TRM, in this case a transducer, that is located at $\vec{r}_j$, will record an impulse response $h(t)$. Due to reciprocity, this means that $G(\vec{r}_r,\vec{r}_s,t) = G(\vec{r}_s,\vec{r}_r,t)$, $h(t)$ is also the impulse response that will be recorded at the source location if the pulse $\delta(t)$ was sent from the transducer location.

The time reversed signal at $\vec{r}_s$ is given by equation (3.11), and it is a common equation use to describe matched filter [41].

$$h(t) * h(-t) \tag{3.11}$$

The result of this convolution will reach its maximum at time $t = 0$ [27]. The maximum is equal to the energy of the signal recorded by the transducer and is given by equation (3.12).

$$\int h^2(t)dt \tag{3.12}$$

There are two qualities of the time reversal process that can be described using match filter theory. The first, is the coherence interference that the waves present when more than one transducer is used. Equation (3.13) represents the time reversed signal at the source when an array is used,

$$\phi(\vec{r}_S, t) = \sum_{r=1}^{r=N} h_r(t) * h_r(-t). \tag{3.13}$$

Each signal in the sum add constructively and reach a maximum at $t = 0$. Uncorrelated contributions that occur at a different time will interfere destructively.

The second, is that time reversal techniques are not susceptible to noise. If the signal that is transmitted from the receiver location has noise in it $h_r(-t) + n_r(t)$ the time reversed signal is then given by equation (3.14).

$$\sum_{r=1}^{r=N} h_r(t) * h_r(-t) + \sum_{r=1}^{r=N} h_r(-t) * n_r(t) \tag{3.14}$$

A sharp peak occurs when the time reversed signal $h_r(-t)$ matches the medium impulse response. Noise, which is not match to the medium, produces low-level background noise that is different from the sharp peak that is produced by the time reversed signal [41].

Chapter 4

Results

4.1 Validation of Time Reversal Analysis

In order to validate the code and the implementation of a time reversal process, a time reversal cavity was analyzed. The progress of the electric field as a function of time was considered. The excitation source is a 2 GHz center frequency Gaussian modulated pulse. The parameters used in the simulations are listed in table 4.1. The Gaussian pulse is propagated in free space and the electric field was recorded on a linear array of receivers. Figure 4.1 shows the simulation geometry. The electric field that was recorded was time reversed and propagated backwards from the receivers' location using the same free space model.

Figure 4.2 shows the progression of the field when is propagated backwards in the model. The back propagated wave starts at time n=1 (20ps) (Fig. 4.2a) and converges at the source at n=108 (2.16 ns) (Fig. 4.2 c). Note that the forward propagating wave at n=75 (1.5 ns)(Fig. 4.2 b), which will focus at the source 66ns later, is a time reversed replica of the wave at n=141 (2.82 ns) (Fig. 4.2 d), which occurs 66ns after focusing at the source.

Table 4.1: Parameters used in the simulations.

Time step (Δt)	Cell Size (Δ)	Pulse Width of Source	Grid Size	Length of array
20ps	1.2cm	16 Δt	249Δ X 249Δ	50Δ

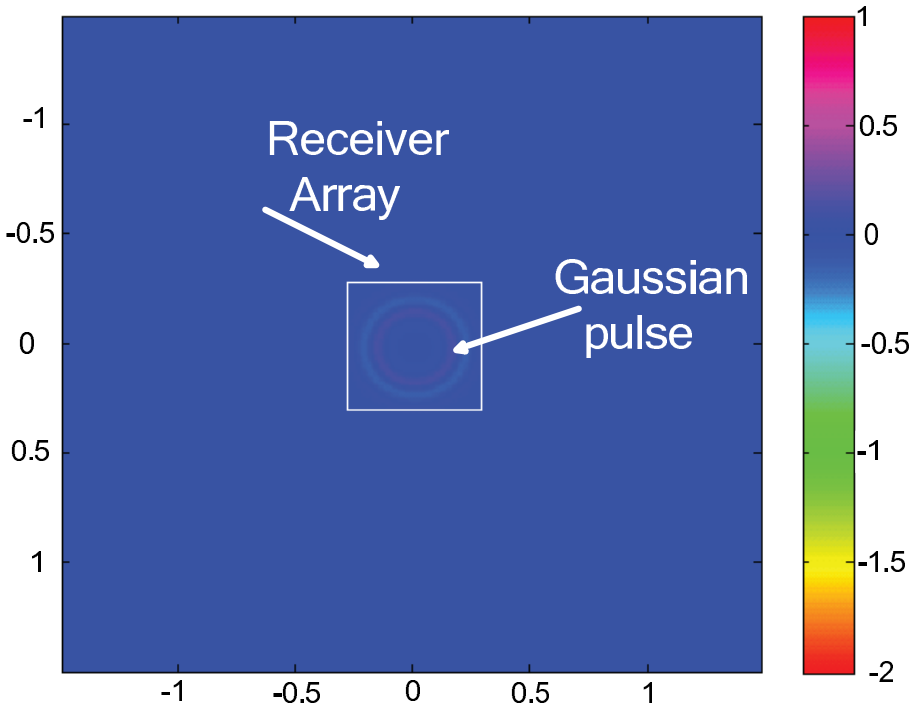

Figure 4.1: Time reversal cavity that shows the receiver array location and the propagation of the Gaussian pulse. "For interpretation of the references to color in this and all other figures, the reader is referred to the electronic version of this dissertation."

4.2 Application of Time Reversal for Defect Imaging

The principles of Time Reversal can be applied to experimentally measured data for defect imaging. A schematic diagram that describes the procedure for imaging is presented in Figure 4.3. Several cases of sample and defect materials were considered.

The simulation geometry considered was a dielectric slab with a relative permittivity (ε_r) of 4 and the excitation source is a modulated Gaussian pulse of 2 GHz center

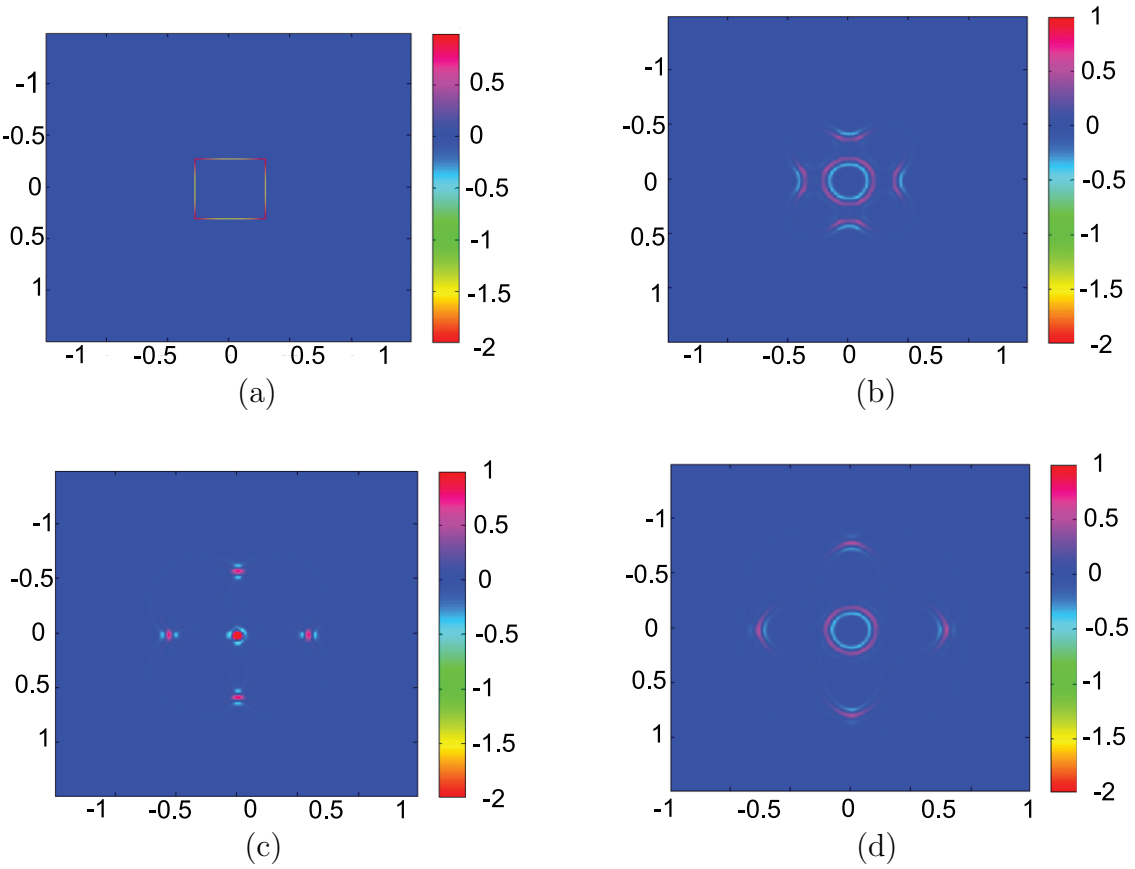

Figure 4.2: Progress of electric field as a function of time when the electric field is propagated backwards in the model. (a) Backpropragated Fields at time 1. (b) Backpropagated Fields at time 75. (c) Backpropagated Fields at time 108. (d) Backpropagated Fields at time 141.

frequency. The parameters used in the simulations are listed in table 4.2. Using a single excitation source the scattered electric field was recorded on a linear array of receivers; time reversed and applied to the simulation model. The model propagates the time reversed signals backwards to highlight the defect. Energy of the propagated field was calculated by integrating the square of the magnitude of the field and the image of the field was displayed. The maxima of the energy image was calculated and its coordinates were compared to the coordinates of the defect.

Table 4.2: Parameters used in the simulations.

Time step (Δt)	Cell Size (Δ)	Pulse Width of Source	Grid Size	Length of array
0.01ns	0.006m	16 Δt	673Δ X 673Δ	500Δ

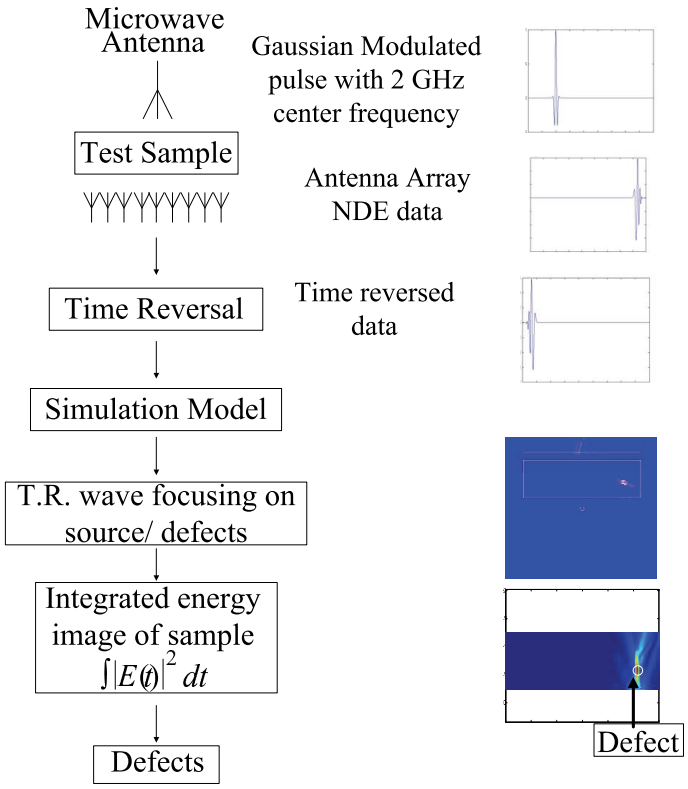

Figure 4.3: A block diagram indicating the procedure that was followed.

4.3 Test 1: Two scatterers in Dielectric Medium

Two air voids in the dielectric slab were simulated. The scatterers had a radius of 0.05m and were placed 6.28λ apart. Figure 4.4a shows the forward propagating wave through the dielectric. Figure 4.4b shows how the time reversed waves focus back on the defects. The energy image in Figure 4.4c shows that the maximum energy for defect 1 occurs at the point (-0.6720m, -0.9300m) while the defect location is at

(-0.7020m,-0.9780m). The maximum energy for defect 2 occurs at the point (1.062m,-0.702m) while the defect location is at (1.0920m,-0.7320m). For defect 1, the distance between the defect location and the energy maximum was 0.7557λ. The distance between defect 2 location and the maximum energy is 0.5664λ. It can be observed through a comparison between the coordinates of the maximum of the energy and the true location of defects that the microwave time reversal technique accurately identifies the location of both defects.

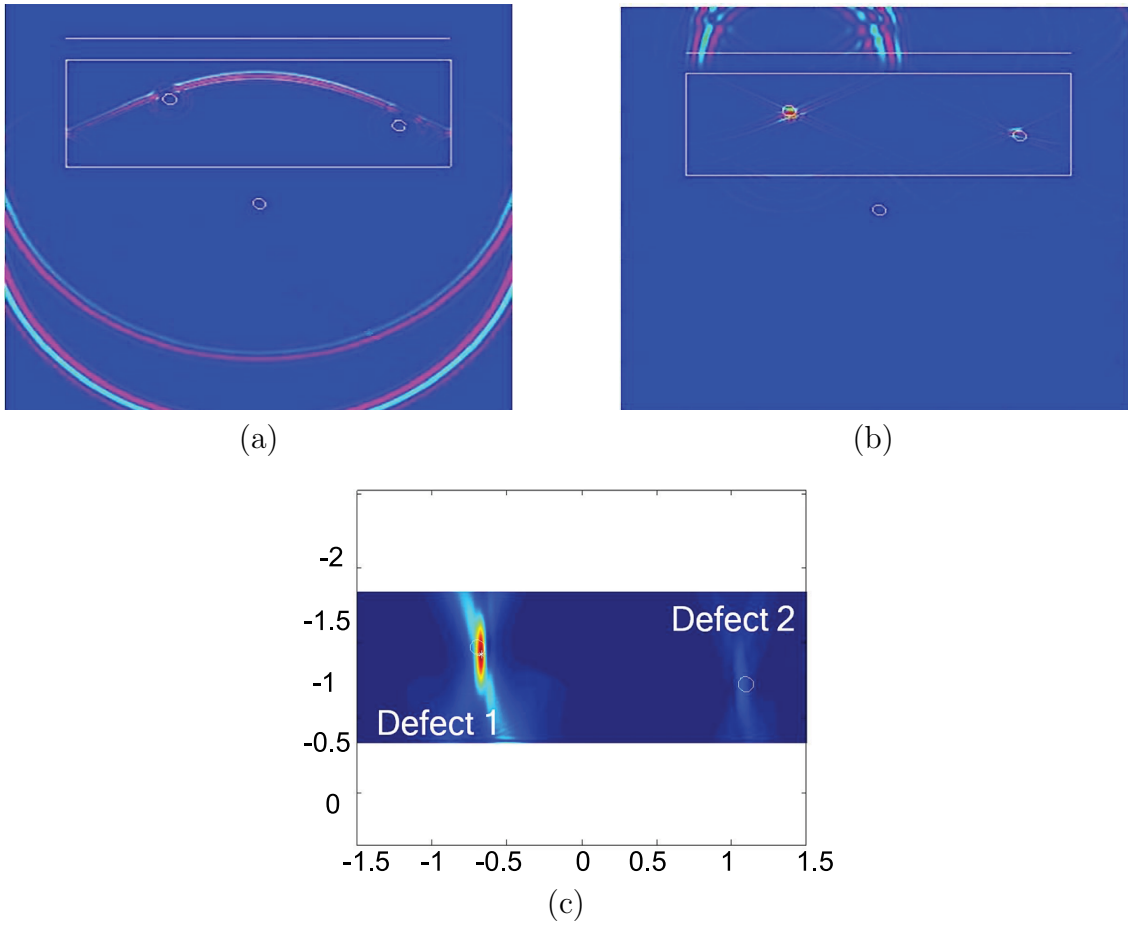

Figure 4.4: Simulations results for two scatterers in a dielectric medium. (a) Forward propagating wave from source. (b) Focusing of time reversed wave on scatterers. (c) Energy images indicating defects location.

4.4 Test 2: Single perfect electric conductor (PEC) Scatterer in Dielectric Medium

A single PEC scatterer in a dielectric slab was simulated. The scatterer had a radius of 0.05m. Figure 4.5a shows how the forward propagating field through the dielectric. Figure 4.5b shows the time reversed wave focusing on the defect. The energy image in figure 4.5c shows that the maximum energy for the defect occurs at the points (1.05m,-0.6900m) while the defect location is at (1.0920m,-0.7320m). The error between the defect location and the maximum energy location was 0.7930λ. The result from the maximum energy coordinate leads us to the conclusion that the microwave time reversal technique accurately identifies the defect in the dielectric material.

4.5 Test 3: Two Scatterers in Dielectric Medium-Resolution of the Model

In order to study the resolution of time reversal imaging, two scatterers 2.27λ apart were considered as shown in figure 4.6. Figure 4.6a shows how the time reversed wave focus on the two defects. Figure 4.6b shows that the maximum energy coordinate and the true location of defect coordinate are very similar. The true location of defect 1 was (-0.8640m,-0.972m) and the maximum energy coordinate was(-0.8460m,-0.930m). Defect 2 was located at (-0.6960m,-0.9720m) while the energy coordinate for defect 2 was (-0.6720m,-0.9240m). For defect 1 the distance between the defect location and the maximum energy location was found to be 0.6λ. For defect 2, the distance between the defect location and maximum energy location was 0.7λ. The technique is able to identify defects that are close together, which indicates the good resolution of the model.

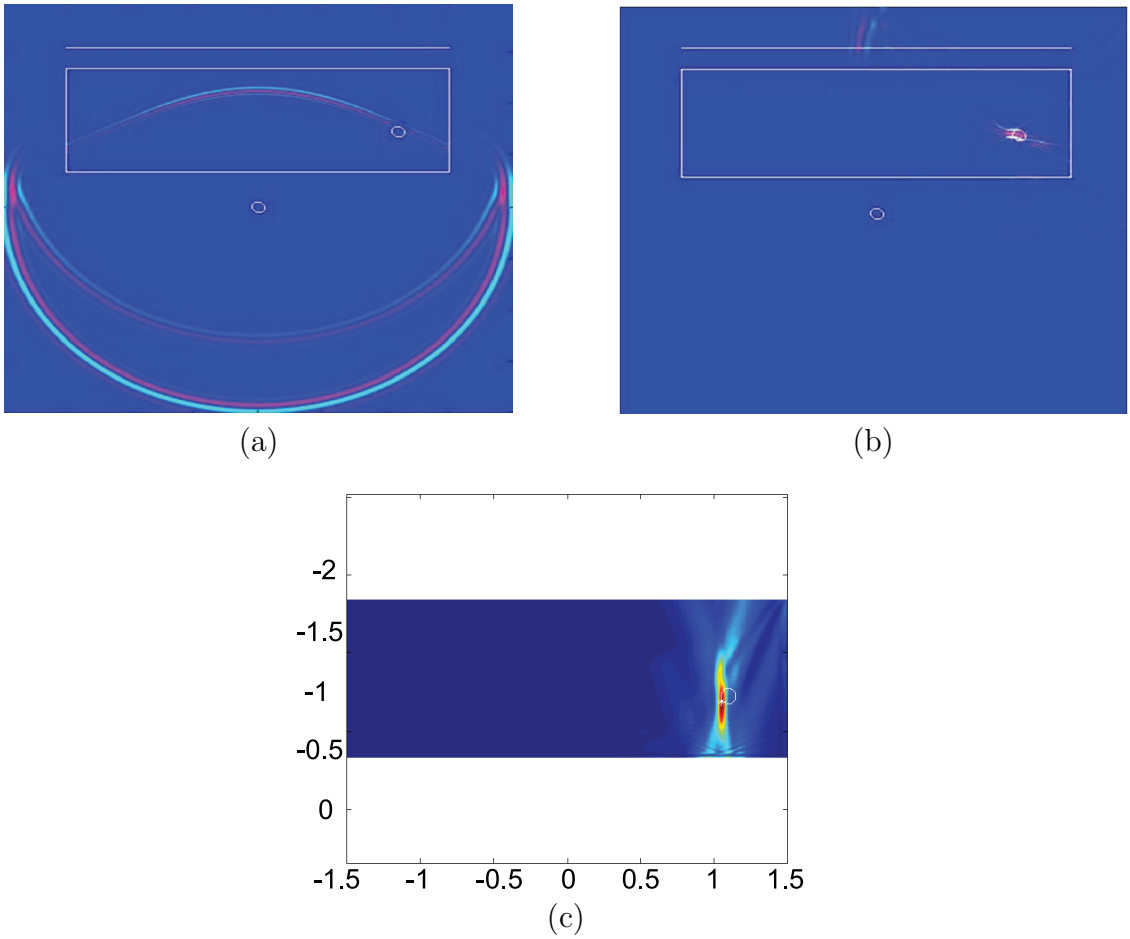

Figure 4.5: Simulations results for single PEC scatterer in a dielectric medium. (a) Forward propagating wave from source. (b) Focusing of time reversed wave on scatterer. (c) Energy image indicating defect location.

4.6 Test 4: Two Scatterers in Dielectric Medium - Reconstruction with noise

In order to evaluate the robustness of the method, the performance was evaluated with noisy "measurements". The simulation geometry consists of two air voids in the dielectric slab placed 6.28λ apart. Random noise with signal to noise ratio (SNR) of 10 was added to the signal measured by the linear array. Fig.4.7(a) shows the time reversed wave focusing back on the defects. The energy image in Fig.4.7(b) shows that the maximum energy for defect 1 occurs at the point (-0.6720m,-0.9300m) while

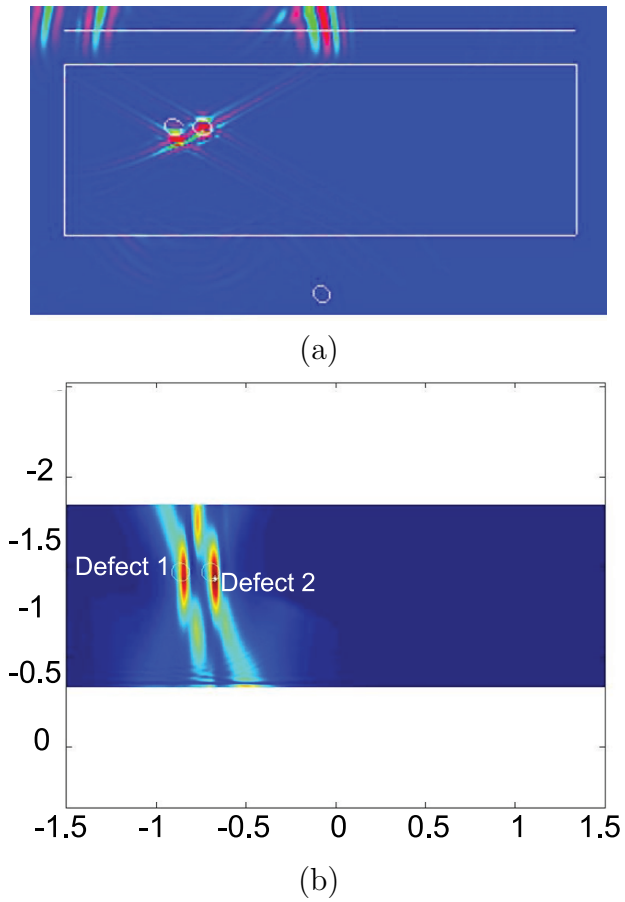

Figure 4.6: Simulations results for 2 scatterers in a dielectric medium 2.27λ apart. (a) Focusing of time reversed wave on scatterers. (b) Energy image indicating location of defects.

the defect location is at (-0.7020m, -0.9780m). The error between the location of the defect and the maximum energy location was calculated to be 0.75λ. The maximum energy for defect 2 occurs at the point (1.1062m,-0.6720m) while the defect location is at (1.0980m, -0.7320m). For the second defect the error between the location of the defect and the maximum energy location was 0.807λ. Figures 4.8 (a) and (b) show the corresponding results when the SNR =2. Defect 1 was located at (-0.7020m, -0.9780m) while the maximum energy occurs at (-0.6720m,-0.9300m). The error between these locations was found to be 0.7547λ. Defect 2 was located at (1.0920m, -0.7320m) while the maximum energy occurred at (1.1062m,-0.6720m). The error between the location of this defect and the location where the maximum

energy occurs was calculated to be 0.82λ. These results clearly demonstrate the robustness of the proposed method.

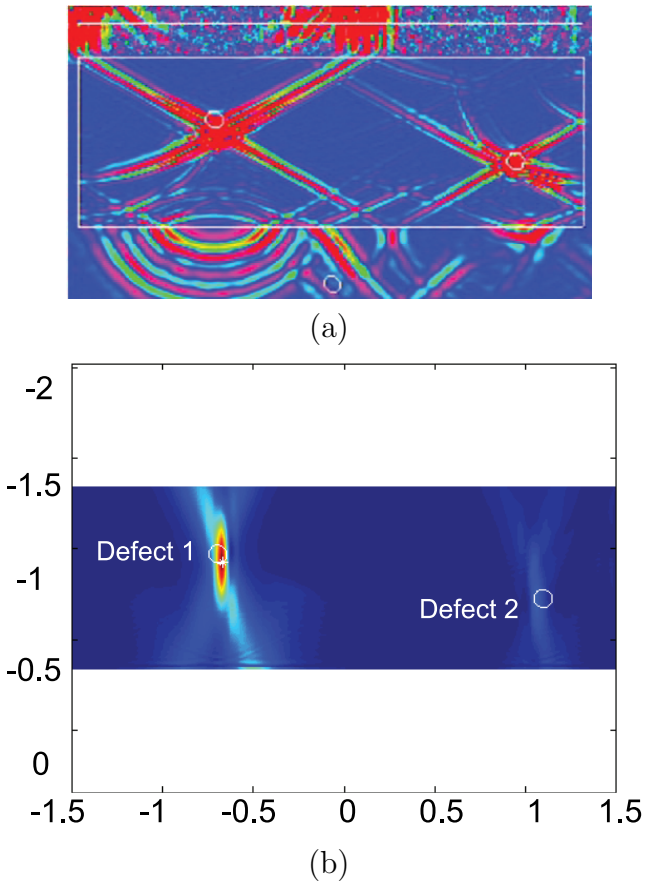

Figure 4.7: Simulations results for 2 scatterers in a dielectric medium 6.28λ apart with noise. (a) Focusing of time reversed wave on scatterers. (b) Energy image indicating location of defects.

4.7 Test 5: Two Scatterers in Dielectric Medium- Two Sources with Noise.

The purpose of this simulation was to improve the SNR of the image with additional sources. It can be seen in Figure 4.9c that the SNR of the energy image is larger than that of the image in Figure 4.7b. The maximum energy for defect 1 occurs at the point (-0.6720m, -0.9420m) while the defect location is at (-0.7020m,-0.9780m). The

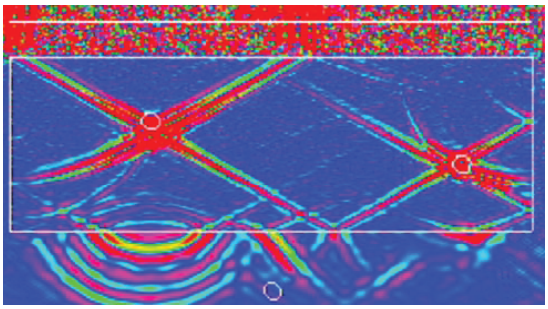

(a)

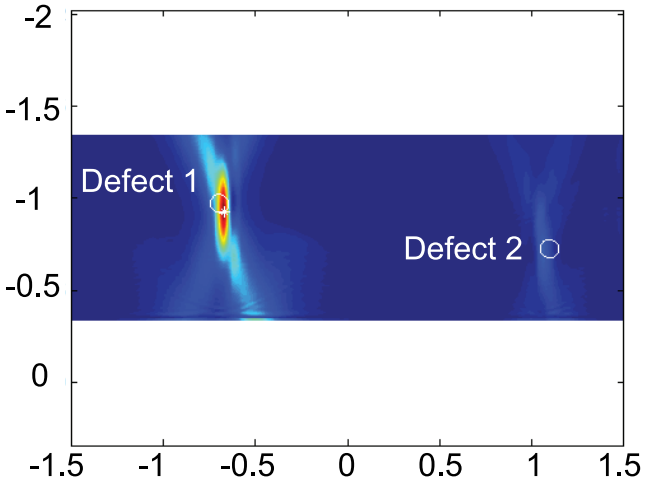

(b)

Figure 4.8: Simulations results for 2 scatterers in a dielectric medium 6.28λ apart with noise. (a) Focusing of time reversed wave on scatterers. (b) Energy image indicating location of defects.

maximum energy for defect 2 occurs at the point (1.08m,-0.666m) while the defect location is at (1.0920m,-0.7320m).

4.8 Test 6: Minimum number of sensors.

The simulation geometry was a dielectric slab with a relative permittivity (ε_r) of 4. The dielectric slab has one air void with a 0.05 m radius. In this simulation the effect of number of receivers on the time reversal process was studied to determine the minimum number of receivers required in an experimental set up to ensure source focusing. The number of receivers was reduced from 500 to 50. The signals from

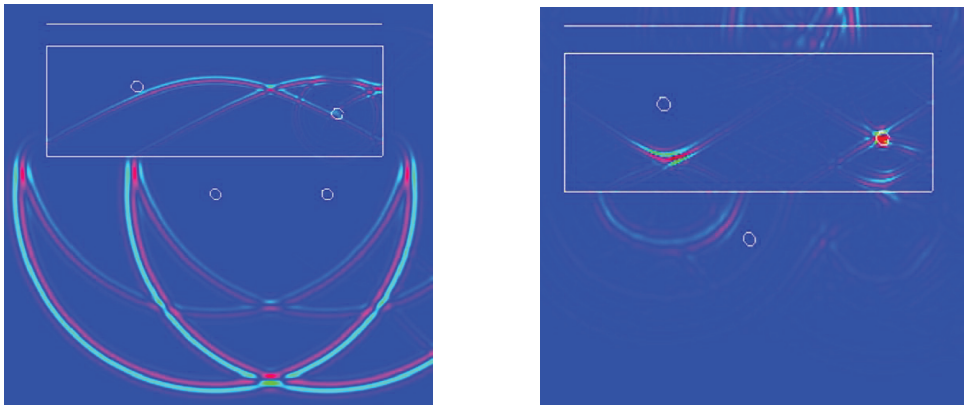

(a) (b)

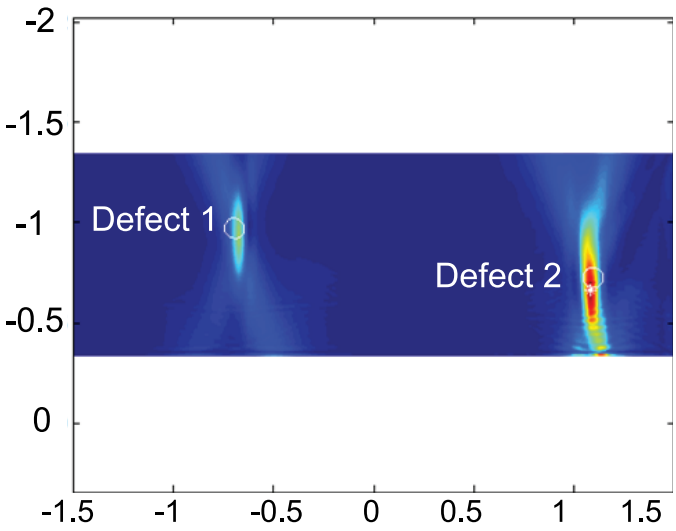

(c)

Figure 4.9: Simulations results for two scatterers in a dielectric medium. (a) Forward propagating wave from the two sources. (b) Focusing of time reversed wave on scatterers. (c) Energy images indicating defects location.

forward propagation are recorded, time reversed and back propagated. The wave focuses on the defect as shown in figure 4.10a. The energy image in figure 4.10b shows that the coordinates of the energy maximum and true coordinates of the defect are similar. The defect coordinates are (-.7020,-.9780) and the maximum energy coordinates are (-.6720,-9240). The error between the two locations is 0.8247λ. The error between the true and estimated locations of the defect when 500 receivers were used, is 0.7557λ. The error is higher when less sensors are used but the defect can

still be detected when 50 sensors are used. The capability of the technique with 50

(a)

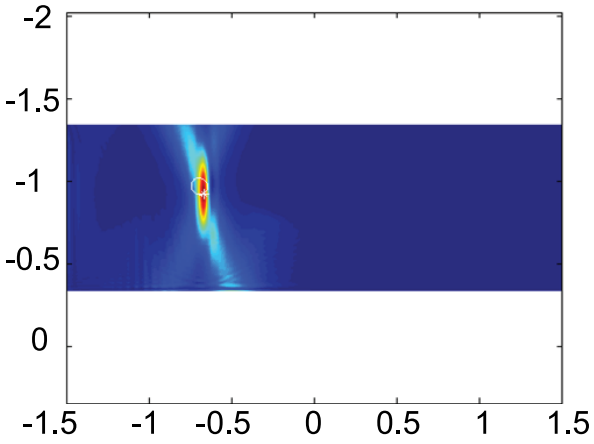

(b)

Figure 4.10: Simulations results for 1 scatterer in a dielectric medium with permittivity of 4. The number of sensors used is 50. (a) Time reversed waves focus on the scatterer. (b) Energy image indicating maximum energy at defect location.

receiving sensors was also tested for the test sample with two scatterers 2.27 apart as shown in figure 4.11. Figure 4.11a shows the time reversed wave focusing on the two defects. Figure 4.12a shows the energy image with the coordinates of the energy maximum. The true coordinate of defect 1 is (-.7020,-.9780) and the coordinate of defect 2 is (-.8700,-.9780). The error between true coordinate and energy coordinate of defect 1 is 2.027λ and for defect 2, the error is 2.76λ. The error between the true and estimated locations of defect 1 when 500 receivers were used, is 0.6λ and for defect 2 is 0.7λ. The error is higher when less sensors are used but the resolution

capability of the model was not affected when 50 sensors are used.

When a random noise of SNR=10 is added to the signal, the results obtained with 50 sensors were able to detect and locate the defects as shown in figure 4.12. Figure 4.12a shows the time reversed waves focusing on the two defects and Figure 4.12b shows the energy image. The true coordinate of defect 1 is (-0.7020,-0.9780) and the energy maximum coordinate is (-0.6720,-0.924). For defect 2, the true coordinate is (1.0920,-0.7320) and the maximum energy coordinate is (1.062,-0.678). The error between the true defect location and maximum energy coordinate for both defects, 1 and 2, is 0.82λ. Figure 4.13a and 4.13b show the corresponding results when SNR = 2. The maximum energy coordinate for defect 1 is (-0.6720,-0.924) and the true coordinate of the defect is (-0.7020,-0.9780). The error between these two coordinates is 0.82λ. The maximum energy coordinate of defect 2 is (1.062,-0.678). The error between these coordinates and the location of defect 2 is 0.82λ. The results show that the model is robust to noise even when fewer sensors are used to record the signals.

The simulations performed with only 50 sensors produced error values higher than those produced when 500 sensors were used. This increase in error values does not affect the capability of the method to detect the defects in the sample.

4.9 Test 7: Time Reversal Applied to Lossy Dielectric Medium.

4.9.1 Two well separated defects.

In this test a sample with finite conductivity and two scatterers was simulated. The scatterers in the simulation have a radius of 0.05m. The simulations were performed for different conductivity values (σ). After the waves were time reversed they were propagated, using the forward model, through the medium with the same ε but

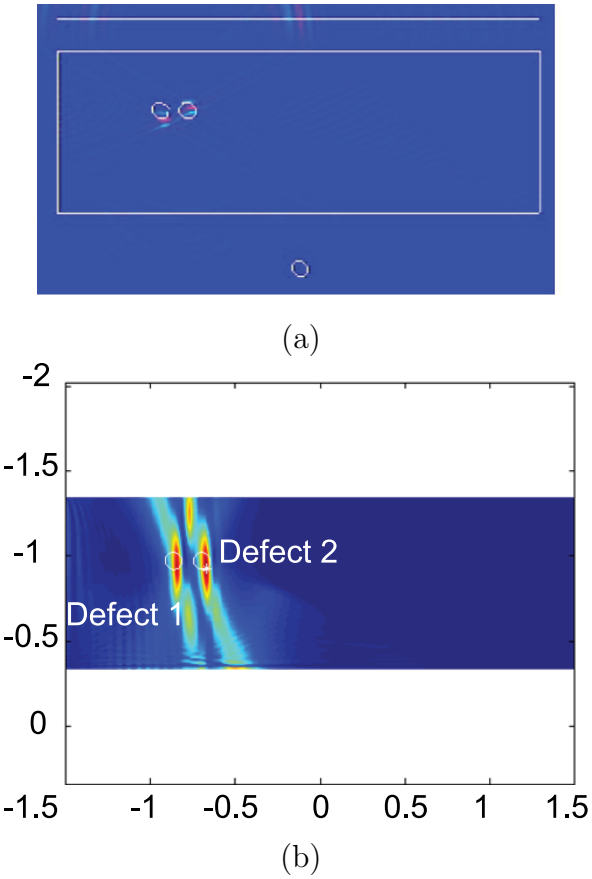

Figure 4.11: Simulations results for 2 scatterer in a dielectric medium 2.27λ apart. The number of sensors used is 50. (a) Time reversed waves focus on the scatterers. (b) Energy image indicating maximum energy at defects location.

the σ=0. Figure 4.14 shows the simulation image for a lossy dielectric slab with conductivity $\sigma = 0.05$ and relative permittivity $\varepsilon = 4$. This image shows how the time reversed wave focuses on the defects. Figure 4.14a shows the energy image obtained from the simulation. The true coordinate of defect 1 is (-0.7020,-0.9780) and for defect 2 is (1.0920,-0.7320). The error between true coordinate and maximum energy coordinate of defect 1 is 0.65λ and between true coordinate and maximum energy coordinate of defect 2 is 0.716λ.

The conductivity values were increased to determine the maximum conductivity value of the material under which the time reversal process can still yield the location of the defect in a lossy test sample. When the conductivity value is chosen as $\sigma = 0.1$

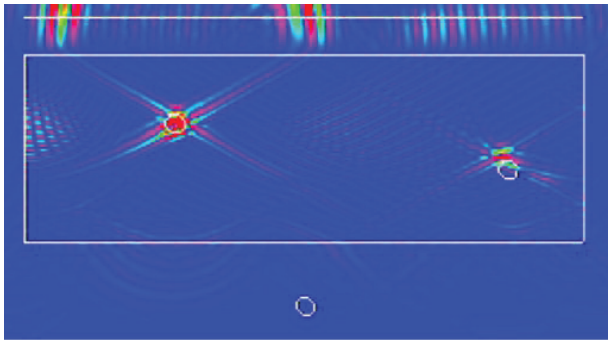

(a)

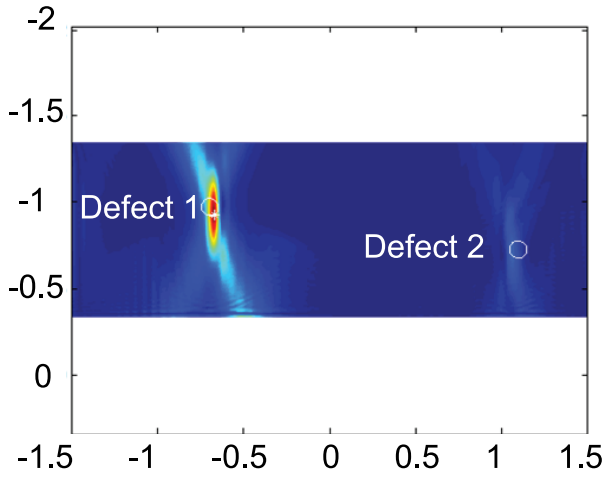

(b)

Figure 4.12: Simulations results for 2 scatterers in a dielectric medium when noise (SNR=10) is added to the recorded signals. The number of sensors used is 50. (a) Time reversed waves focuses on the 2 scatterers. (b) Energy image indicating maximum energy at defect location.

the attenuation of the wave decreases the intensity values of the wave as shown in figure 4.15a. The intensity of the wave is low and the time reversed wave does not focuses in the defects. Figure 4.15b shows the energy image obtained from the simulation. The true coordinate of defect 1 is (-0.7020,-0.9780) and for defect 2 is (1.0920,-1.20). The error between true coordinate and the coordinate of maximum energy of defect 1 is 0.4 λ. The error between true coordinate and maximum energy coordinate of defect 2 is 0.24λ.

The simulation was repeated with sample conductivity $\sigma = 0.2$. The waveform

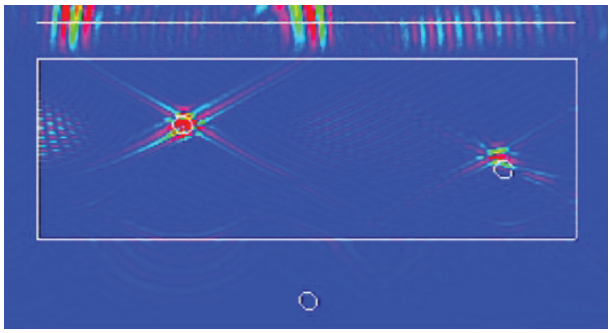

(a)

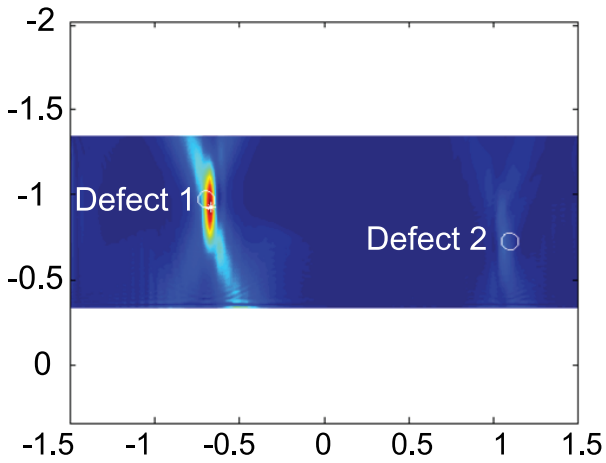

(b)

Figure 4.13: Simulations results for 2 scatterers in a dielectric medium when noise (SNR=2) is added to the recorded signals. The number of sensors used is 50. (a) Time reversed waves focuses on the 2 scatterers. (b) Energy image indicating maximum energy at defect location.

does not focuses on the defects in figure 4.16a. Figure 4.16b shows the energy image obtained from the simulation. The energy image shows that there is only one maximum, which occurs at (1.098,-1.224). The true defect coordinate is (1.0920,-1.2020) and the error between the true coordinate and the coordinate of maximum energy is 0.3040λ. When this defect is moved to position (1.0920,-0.7320) neither of the defects can be detected as shown in figure 4.16c. It can be concluded that at a conductivity $\sigma = 0.2$ the attenuation is too severe for the technique to detect the defects.

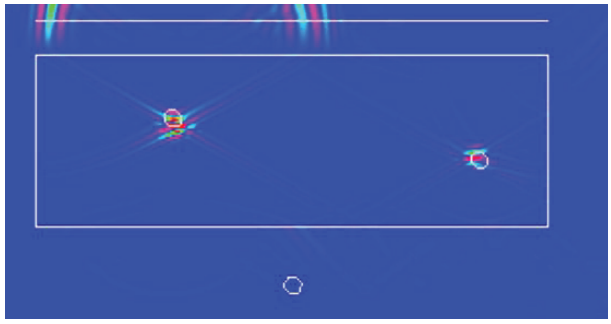

(a)

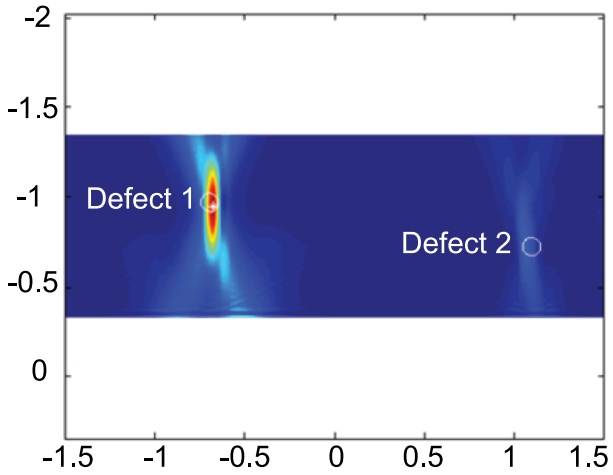

(b)

Figure 4.14: Simulations results for 2 scatterers in a lossy dielectric medium when σ=0.05. (a) Time reversed waves focuses on the 2 scatterers. (b) Energy image indicating maximum energy at defect location.

4.9.2 Closely placed defects.

Two scatterers 2.27λ apart were considered to further test the accuracy of time reversal imaging, when lossy dielectrics were used as samples. A conductivity σ=0.05 and permittivity ε=4 were used in the simulation. The time reversed waves focus on the defects as shown in figure 4.17a. Figure 4.17b shows the energy image and it is seen that the maximum energy coordinates and the true coordinates of defects are very similar. Defect 1 is located at (-0.7020m,-0.9780m) while the coordinate of maximum energy is located at (-0.8520m,-0.9360m). The error between these two coordinates is 2.08λ. Defect 2 is located at (-0.8700m,-0.9780m) while the maximum

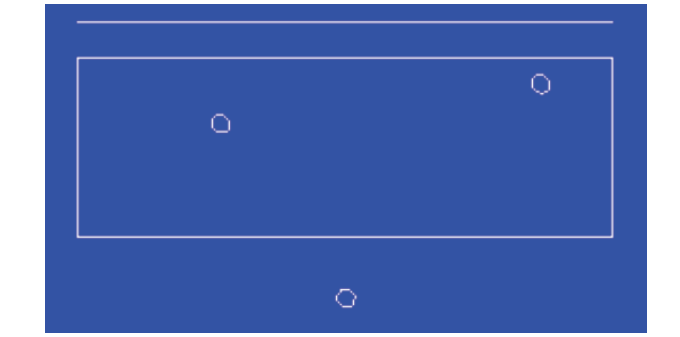

(a)

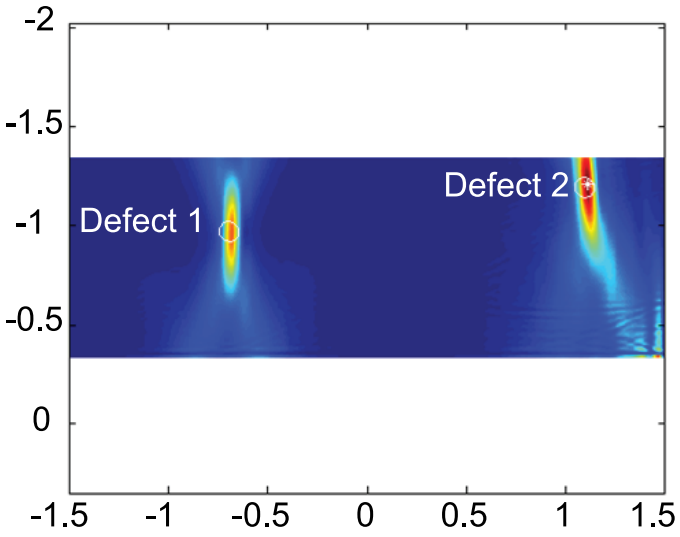

(b)

Figure 4.15: Simulations results for 2 scatterers in a lossy dielectric medium when σ=0.1. (a) Time reversed waves focuses on the 2 scatterers. (b) Energy image indicating maximum energy at defect location.

energy coordinate is located at (-0.6780m,-0.9540m). The error between these two coordinates is 2.68λ.

The simulation was performed next with a higher conductivity σ=0.08. In lossy dielectrics, the waves are attenuated as figure 4.18a shows. Figures 4.18b and 4.18c show that the wave is affected by attenuation and not by dispersion. Due to attenuation the wave does not focus on the defect location, as shown in figure 4.19a. The true coordinate of defect 1 and 2 are (-0.7020m,-0.9780m) and (-0.8700m,-0.9780m), respectively. The error between true and estimated locations of defect 1 is 2.08λ. The error between true and estimated locations of defect 2 is 2.68λ. The simulation

(a)

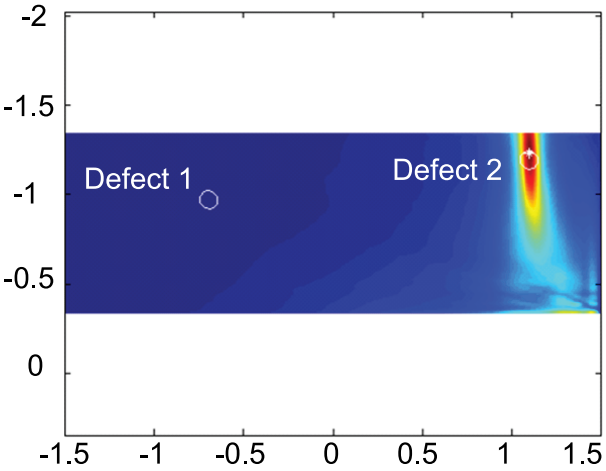

(b)

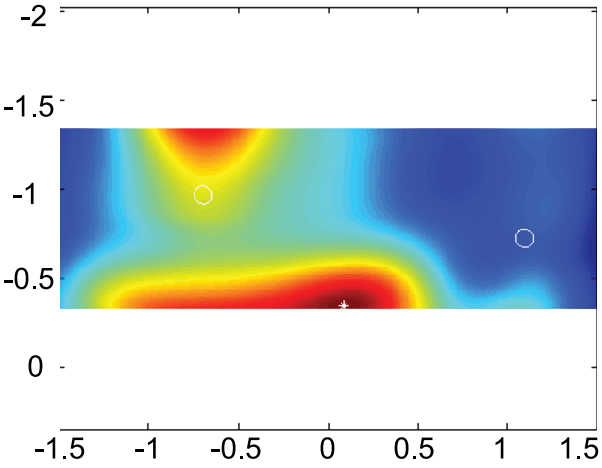

(c)

Figure 4.16: Simulations results for 2 scatterers in a lossy dielectric medium when σ=0.2. (a) Attenuated time reversed waves. (b) Energy image indicating maximum energy at defect location. (c) Energy image indicating maximum energy location.

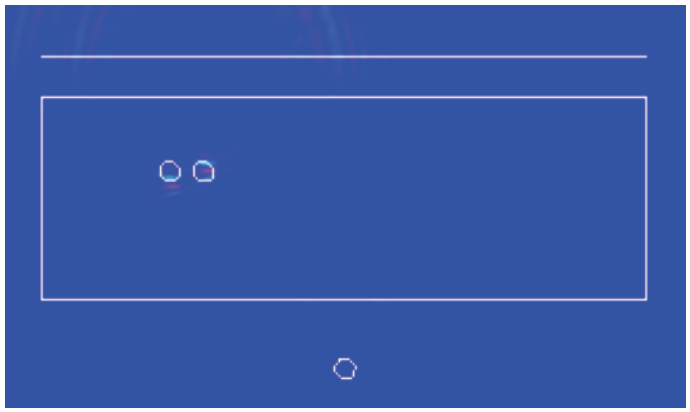

(a)

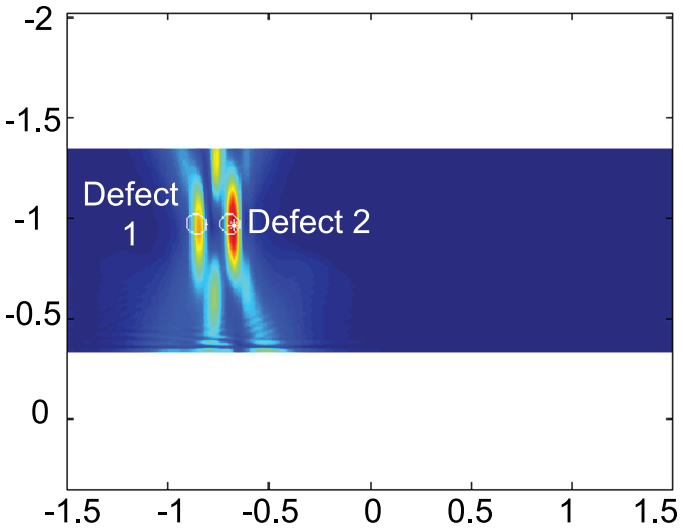

(b)

Figure 4.17: Simulations results for 2 scatterers 2.27 λ apart in a lossy dielectric medium when σ=0.05. (a) Attenuated time reversed waves. (b) Energy image indicating maximum energy at defect locations.

was then performed with a conductivity σ=0.2 and permittivity ε=2.9. Figure 4.20 shows that the energy maximum does not occur at the true defect location. When the material has a conductivity σ=0.2 and a permittivity ε=2.9 the defects can not be detected.

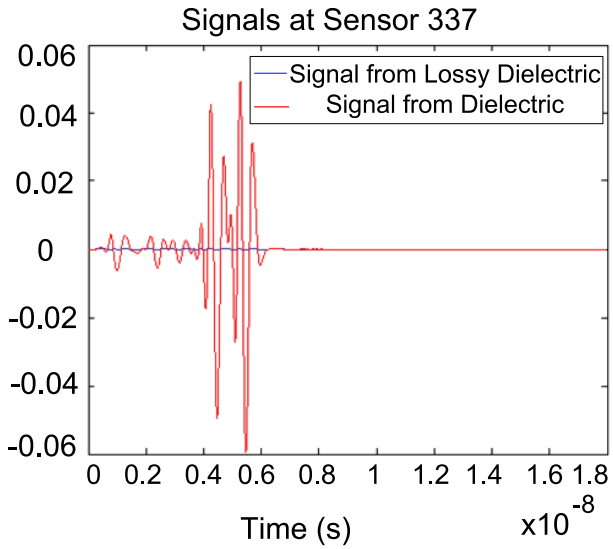

(a)

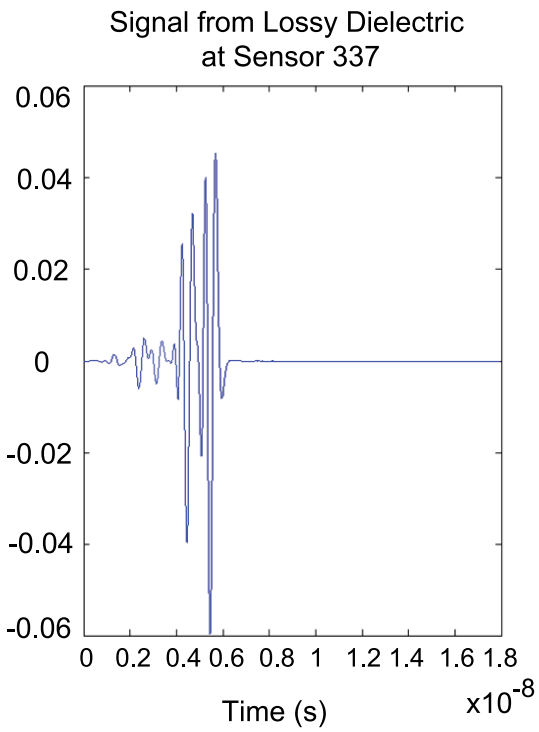

(b)

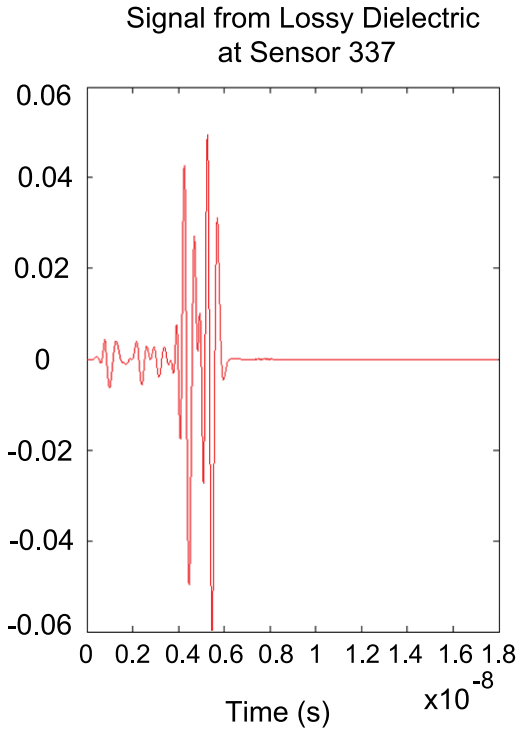

(c)

Figure 4.18: Attenuation effects from the conductivity (σ=0.08) of the material for 2 scatterers 2.27 λ apart. (a) Comparison between signal from sensor 337 for a lossy dielectric and a dielectric. (b) Signals from sensor 337 for a lossy dielectric. (c) Signals from sensor 337 for a pure dielectric.

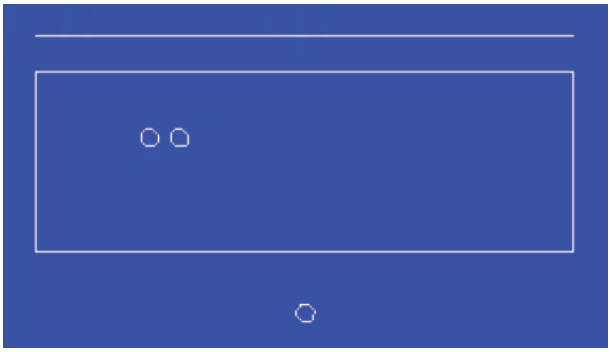

(a)

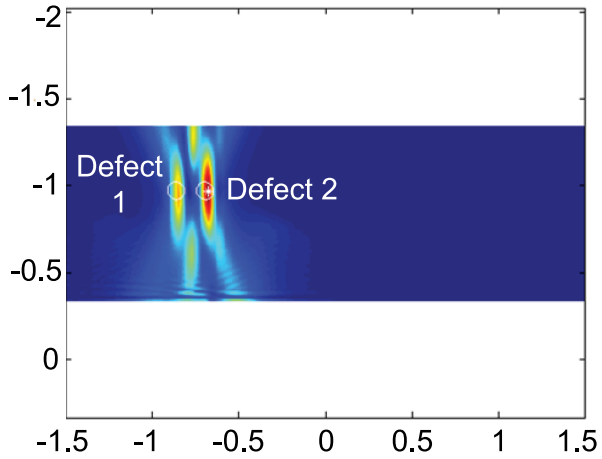

(b)

Figure 4.19: Simulations results for 2 scatterers 2.27 λ apart in a lossy dielectric medium when σ=0.08. (a) Attenuated time reversed waves. (b) Energy image indicating maximum energy at defect locations.

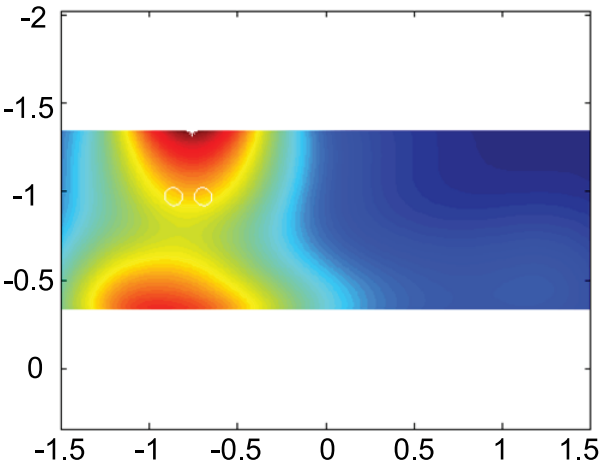

Figure 4.20: Energy image for 2 scatterers 2.27 λ apart in a lossy dielectric medium when σ=0.2 and ε=2.9.

4.10 Test 8: Effect of errors in receiver measurements.

4.10.1 Error in time measurements.

Two different test were conducted to determine effect of error in time measurements of the receiver array signals. The errors were introduced in the form of time delays in the received signals which were then time reversed and back propagated using the FDTD model. The simulation was performed in free space and the source was located at position (0,0). The first test consisted of changing the time delay in randomly selected receiver signals using pseudorandom values obtained from the standard uniform distribution. The maximum time delay introduced to the signals was 175 Δt and the minimum value was 90 Δt. The source field field was recorded at 51 sensors positions, was time reversed after time delays were selectively introduced in some signals.

Signals at all 51 sensors positions, placed along the x axis, were time delayed by random quantities. The resulting A-scan signals of each receiver in the array, after introducing random time delays are shown in figure 4.21. The energy image in figure 4.22 shows the position where the maximum of the back propagated energy occurs. The coordinates where the maximum occurs are (0.0060,-0.0840). The error between the coordinate of maximum energy and the true source coordinate is 0.56λ. This error is higher than the error of 0.08λ without any error in time delay.

The simulation was repeated but only 46 signals were modified. The 5 signals, that were not modified, were at positions -0.6, -0.54, -0.48, -0.42, -0.36 m. The A-scan signals of each receiver in the array, after introducing random time delays are shown in figure 4.23. The energy image in figure 4.24 shows that the maximum energy position occurs at (0.0060,0.0720). The error between the coordinates of maximum energy and the true coordinates is 0.62λ.

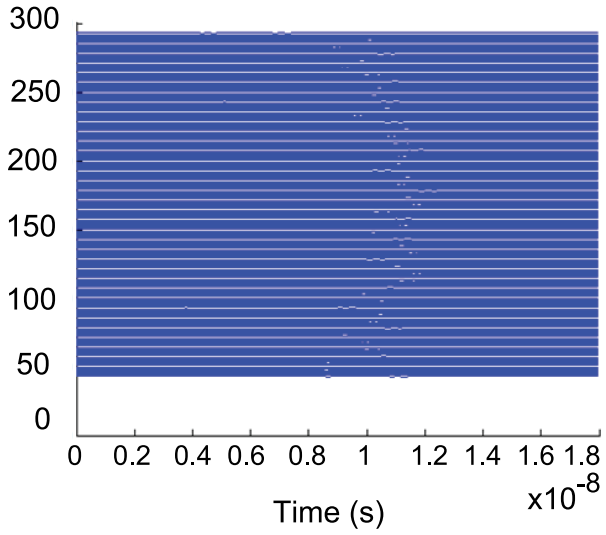

Figure 4.21: Individual A-scan signals at the receiver when the time delay is modified.

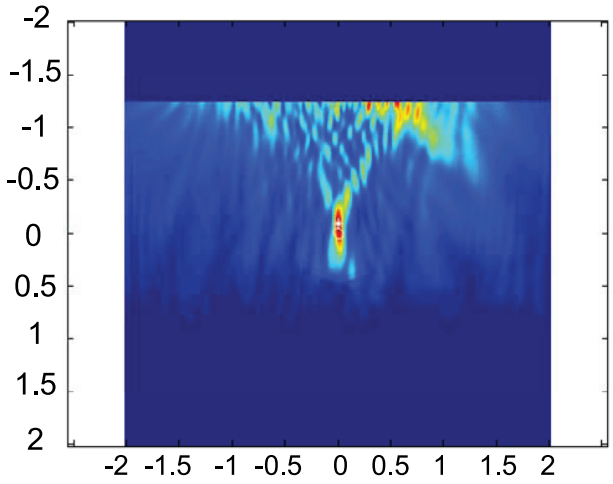

Figure 4.22: Energy image when signals at all positions were delayed by random quantities.

The number of sensors, which signals were delayed, in the next test was kept at 46. The same 46 signals used in the last test were used for this test. In this test the amplitude of the 46 signals was modified by multiplying the signals by a factor based on pseudorandom values obtained from the standard uniform distribution. The factors varied from 0.90 to 0.99. The A-scan signals, after the time delay and amplitude were modified, are shown in figure 4.25. The coordinates where the energy maximum occurs is (0.0060,0.0780), as shown in figure 4.26. The error increased to

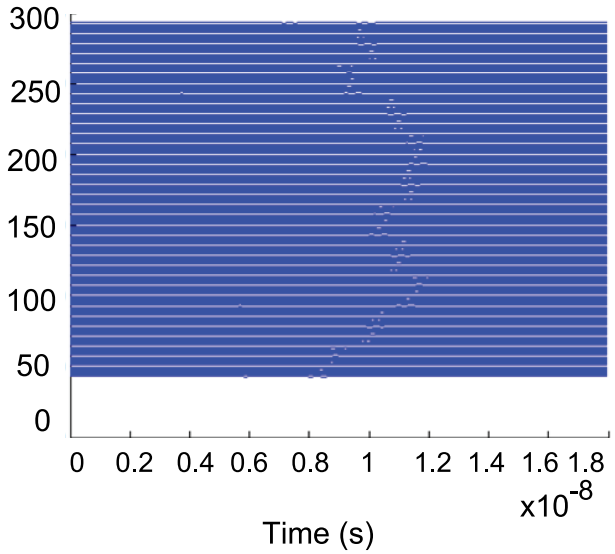

Figure 4.23: Individual A-scan signals at the receiver when the time delay is modified.

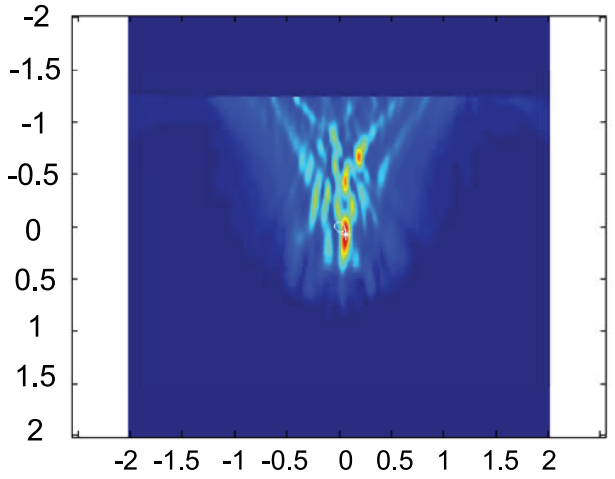

Figure 4.24: Energy image when 46 signals were modified.

0.68λ when the amplitude of the signals was modified. The energy images presented in this section show that changes in time delay in the signals greatly affect focusing of the back propagating wave and estimation of source location. In all the cases the waves focus near the source location but not on the source location.

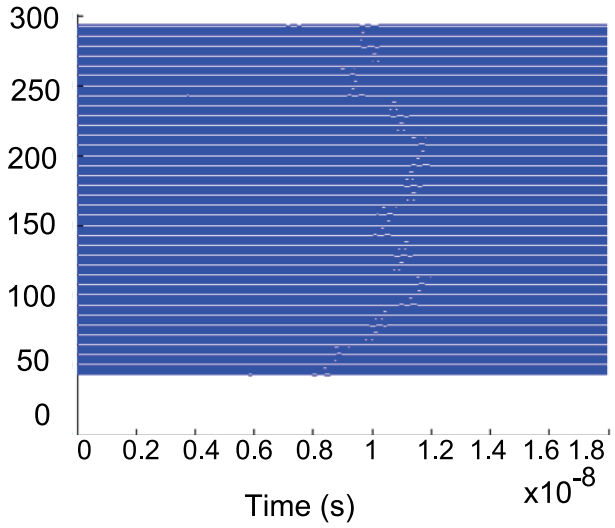

Figure 4.25: Individual A-scan signals at the receiver when the time delay and amplitude are modified.

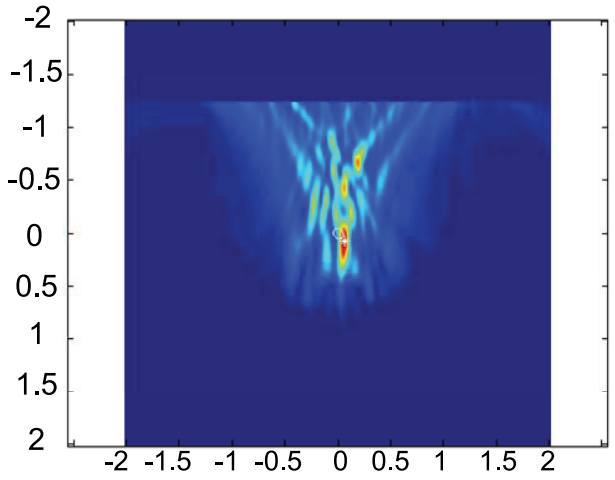

Figure 4.26: Energy image when 46 signals were modified.

4.10.2 Error is Transducer Position.

The second type of test consisted in simulating an error in transducer position. When the sensors in the x coordinate are not ideally placed at locations specified in the simulation model, the use of the model in back propagation can result in errors. This study was conducted with 40 sensors as is the case with the experiment performed. The simulation was performed in free space. The sensors were located 2 m away from the source position. The true coordinates of the source are (0.002,-0.022). The

estimated source position can be identified from the energy image, as shown in figure 4.27.

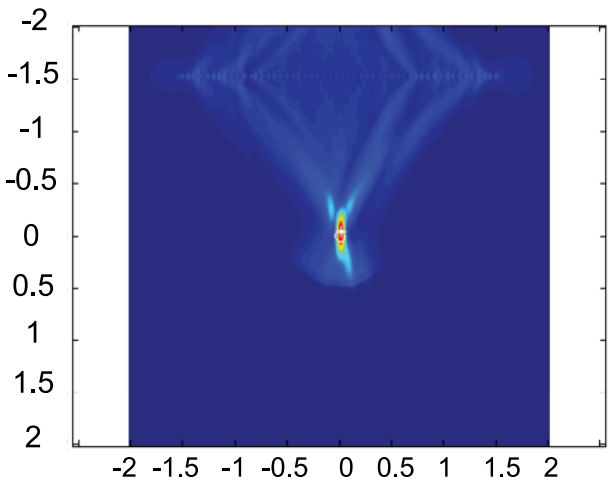

Figure 4.27: Energy image when time delay is simulated using sensor position error.

In conclusion, the results presented in these sections show that:

- Changes in amplitude and time delay increased detection error.
- Time delay differences created by position errors in the x coordinate did not affect the focusing capability of the model.
- The time delay due to position errors caused small changes in time delay.

4.11 Test 9: Results with different sensor locations

Simulations, using different number of sensors and location in space, were performed to document the performance under different spatial distributions of sensors. The first test was performed using 11 sensors, equally spaced, in the x coordinate from a distance of -1.5 to 1.5 m. The energy image and a snapshot of the movie, presented in figures 4.28, 4.29 respectively, show how the wave focuses on the source position. The individual A-scan signals acquired in the sensor positions are shown in figure 4.30.

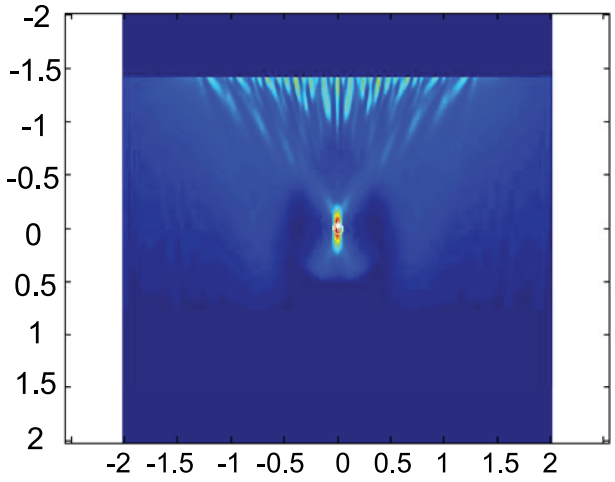

Figure 4.28: Energy image when 11 sensors from a distance of -1.5 to 1.5 m were used in the simulation.

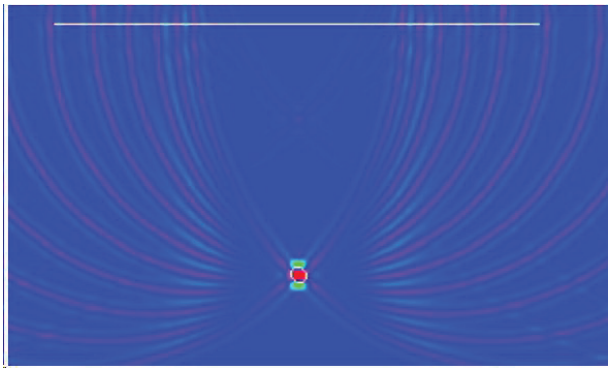

Figure 4.29: Snapshot from movie showing the place where the waves focus.

The number of sensors were decreased from 11 to 6. The sensors were placed, in the x position, from -1.5 to 1.5 m. Reducing the number of sensors did not affect the focusing capabilities of the model, as shown in figures 4.31, 4.32. The A-scan signals at the 6 sensors are shown in figure 4.33. The spatial extent of the receiver array was reduced to determine if this change affects the focusing capabilities of the model.

Next, the spatial extent of the receiver array was reduced to the area between -0.6 to 0.6 m. The number of sensors used was reduced to 5. Individual A-scans signals at the receivers are shown in figure 4.34. The snapshot taken from the movie file, in figure 4.35, shows the focusing point is wider than the one in figure 4.32. The energy image in figure 4.36 shows the location of the defect but the energy is spread over the

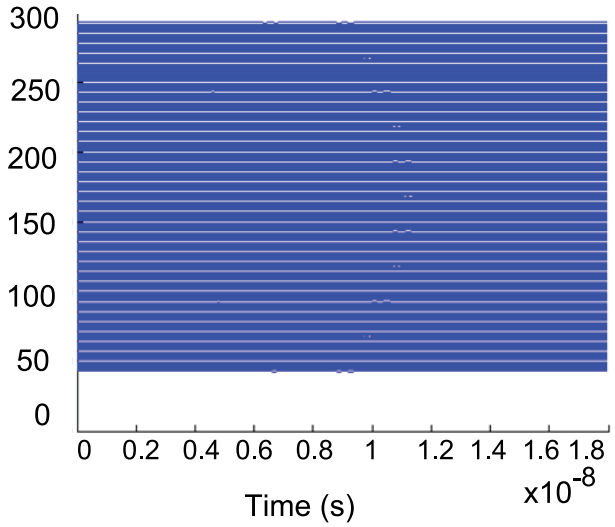

Figure 4.30: Individual A-scan signals at the receivers.

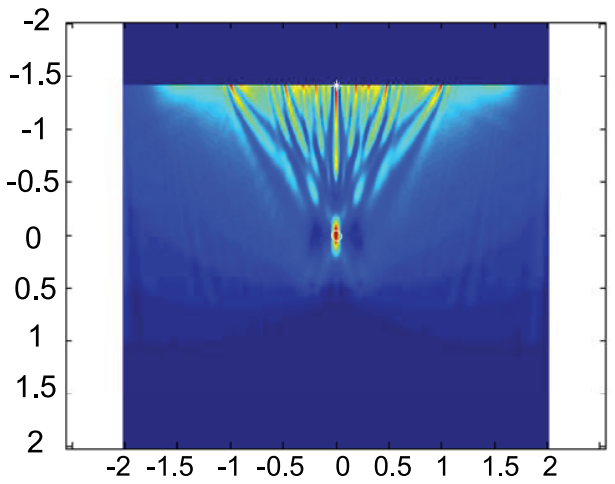

Figure 4.31: Energy image when 6 sensors from a distance of -1.5 to 1.5 m were used in the simulation.

location of the source.

The A-scan signals of the receiver signals when the spatial extent is reduced to the area from -0.5 to 0.5 m, are shown in figure 4.37. The waves do not focus in the source position as shown in figure 4.38. As a result of this, the energy is spread in the depth direction although the location in x-direction is fairly accurate as seen in figure 4.39. The same observations are made when the spatial distance of the receiver array is reduced to the area from -0.45 to 0.45 m. The number of sensors used for

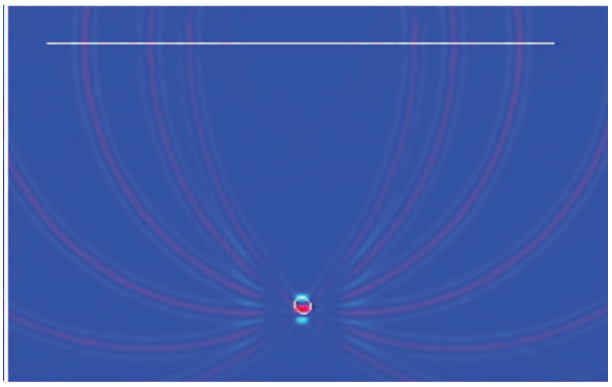

Figure 4.32: Snapshot from movie showing the place where the waves focus.

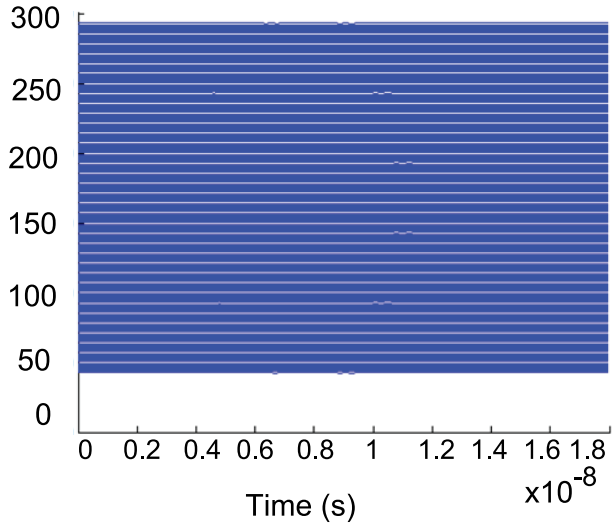

Figure 4.33: Individual A-scans signals at the receiver.

this test were 7. The A-scan are shown in figure 4.40. The waves do not focus at the source location, as seen in figure 4.41 and in the energy image in figure 4.42.

The number of sensors used in the simulations did not affect the focusing capability of the model. However, the distance covered by the sensors affected the focusing capabilities of the model. The source position can not be detected when the receiver array covers a small area on the receiver plane that does not capture the wave characteristics of the data as seen when the distance covered by the sensors is reduced to -0.6 to 0.6 m, to -0.5 to 0.5 m, and to -0.45 to 0.45 m.

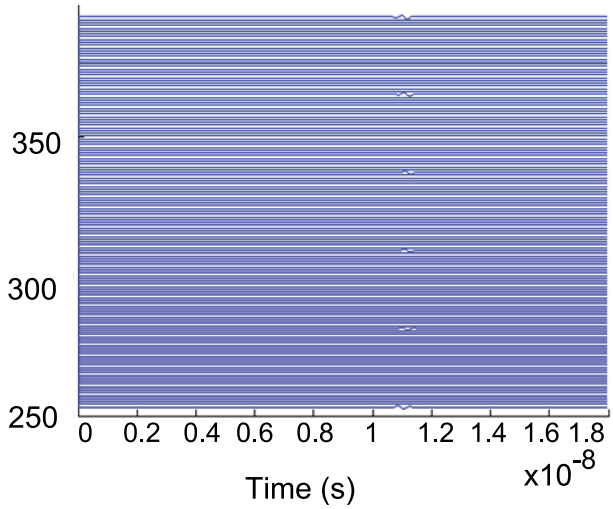

Figure 4.34: Individual A-scans signals at the receivers.

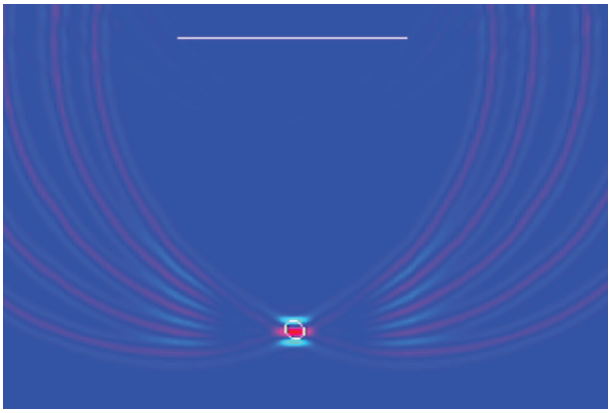

Figure 4.35: Snapshot from movie showing the place where the waves focus.

4.12 Test 10: Distances from the source to the sensor array.

Simulations, using different distances from transmitter position to receiver position, were performed to understand if this distance affected the focusing capabilities of the model. The distance between the transmitter and the central receiver, used for the first simulation, was 1 m. The number of sensors used for this simulation were 6. The distance covered by the sensors was from -1.5 to 1.5 m, in the x axis, for all the simulations. The energy image, in figure 4.43, shows that the wave focuses on the

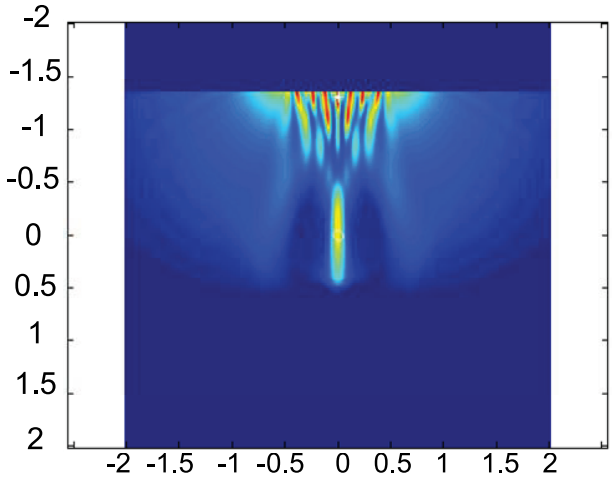

Figure 4.36: Energy image when 5 sensors from a distance of -0.6 to 0.6 m were used in the simulation.

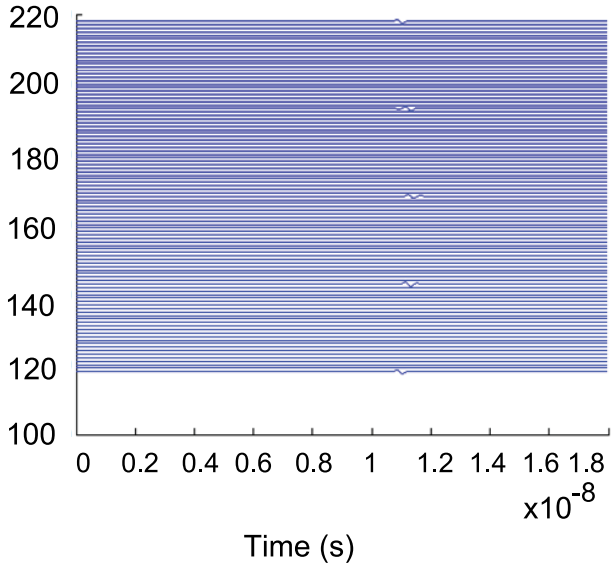

Figure 4.37: Individual A-scan signals at the receivers.

source original location.

The distance between transmitter and the central receiver was decreased to 0.7 m. The number of sensors, used in all test in this section, is 11. The energy image, in figure 4.44, shows the wave focusing on the source position. The simulation is repeated decreasing the distance between transmitter and receiver to 0.5 m and 0.2 m. The energy image, for the 0.5 m case, in figure 4.45, shows that the maximum of the energy occurs at the source location. The same results, for the 0.2 m case, can

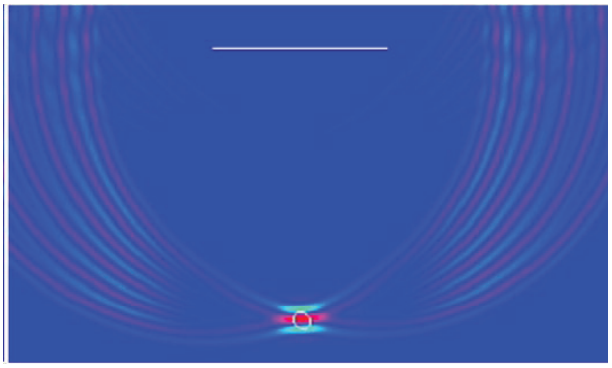

Figure 4.38: Snapshot from movie showing the place where the waves focus.

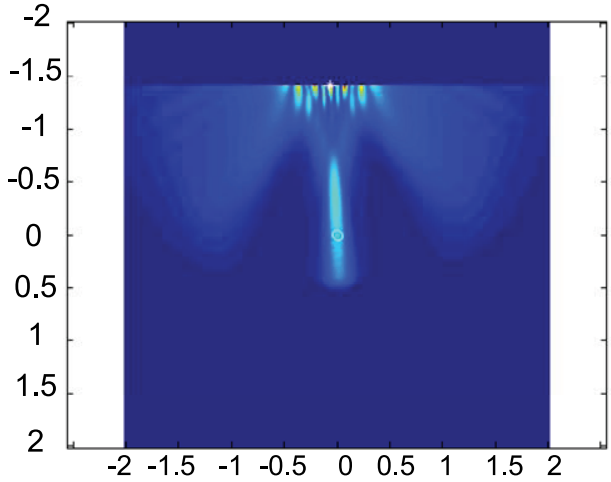

Figure 4.39: Energy image when 6 sensors from a distance of -0.5 to 0.5 m were used in the simulation.

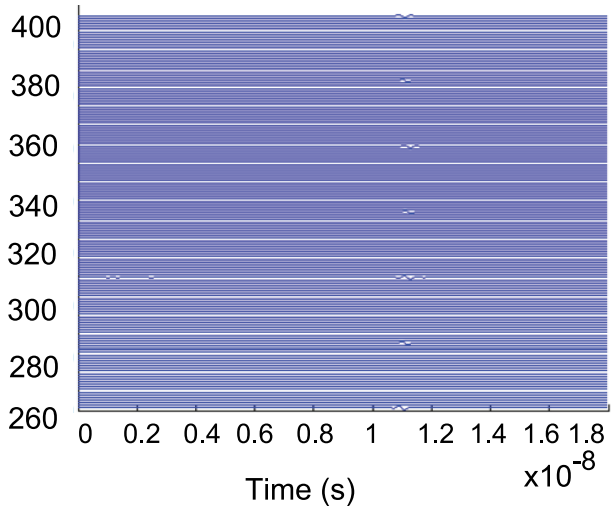

Figure 4.40: Individual A-scan signals at the receivers.

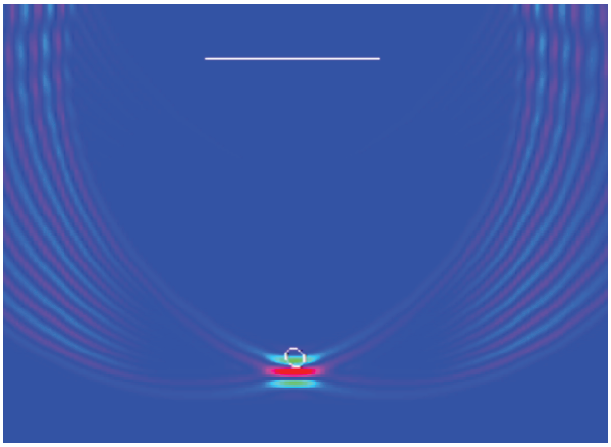

Figure 4.41: Snapshot from movie showing the place where the waves focus.

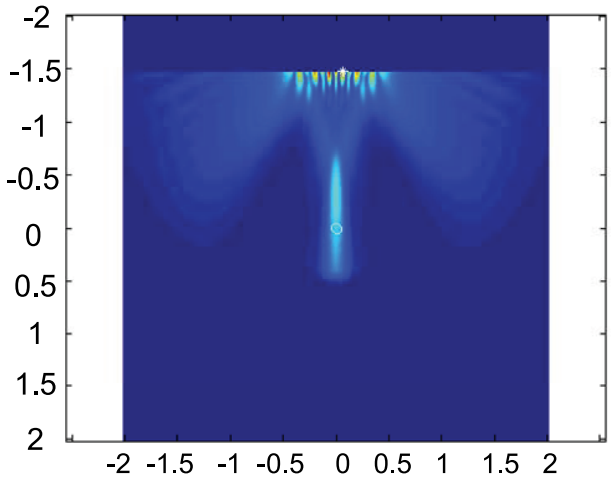

Figure 4.42: Energy image when 7 sensors from a distance of -0.45 to 0.45 m were used in the simulation.

be observed in figure 4.46. The distance between the transmitter and receivers does not affect focusing of the wave in the source location.

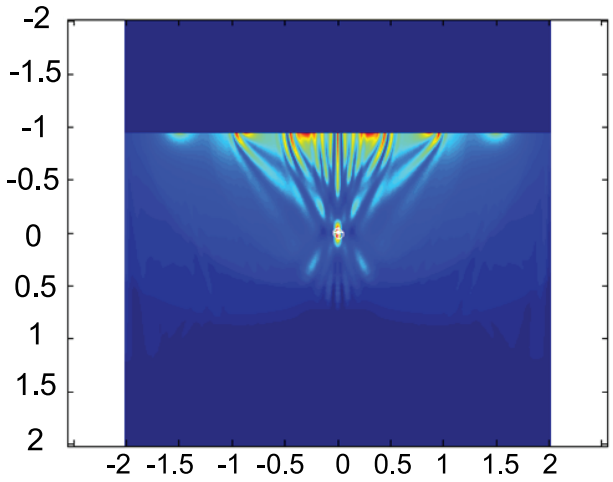

Figure 4.43: Energy image when the sensors are 1 m away from the source location.

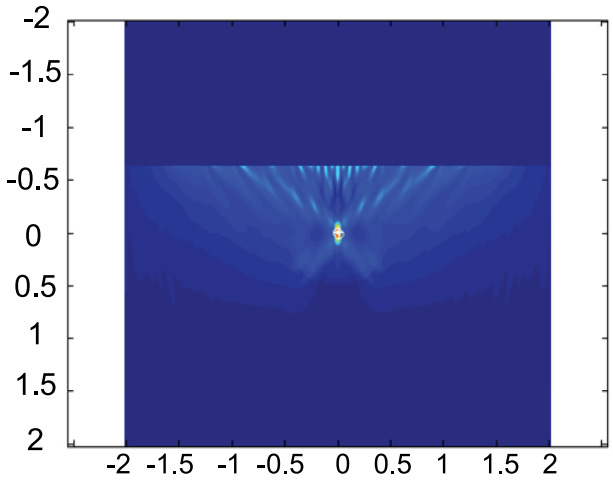

Figure 4.44: Energy image when the sensors are 0.7 m away from the source location.

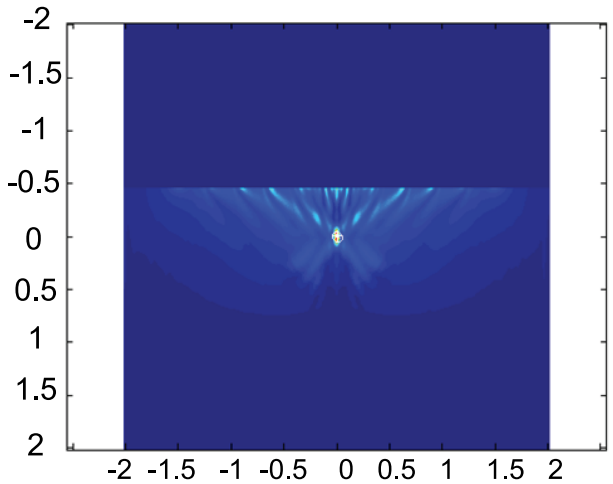

Figure 4.45: Energy image when the sensors are 0.5 m away from the source location.

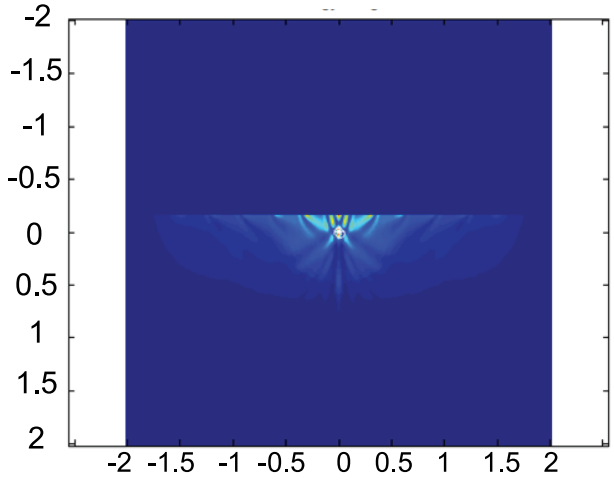

Figure 4.46: Energy image when the sensors are 0.2 m away from the source location.

Chapter 5

Experiment

This chapter describes the experimental validation results of time reversal techniques applied to experimental microwave NDE data. First, an experiment was set up to validate the simulation results obtained using the FDTD model. Transmission measurements from a microwave source in air were performed in time domain to validate the simulation model. Two TEM horn antennas, a pulse generator, and an oscilloscope were used in the experiment set up. One of the antennas was used as a transmitter and the receiving antenna was moved to emulate a linear array of receivers that is used in the simulations. The measured data was recorded, time reversed, and input into the FDTD model to validate it. An energy image with the experimental data was generated and compared to the energy image produced using simulated data.

5.1 Experiment Set Up

The experiment set up used is shown in figure 5.1. The experiment was performed in free space constituting a homogeneous medium in the solution domain. Two H-1498 TEM horn antennas, manufactured by American Electronic Laboratories were used. Each antenna had a bandwidth of 2 to 18 GHz so that the average wavelength, λ=0.1.

The transmitter antenna was placed on the arch range and the receiver antenna was placed in a moving cart shown in figures 5.2 and 5.3, respectively. Two different experiments were performed. In the first experiment the antennas were placed 1.96 m or 19.6λ away as shown in figure 5.4. In the second experiment the antennas were placed 2.90 m or 29λ away as shown in figure 5.5.

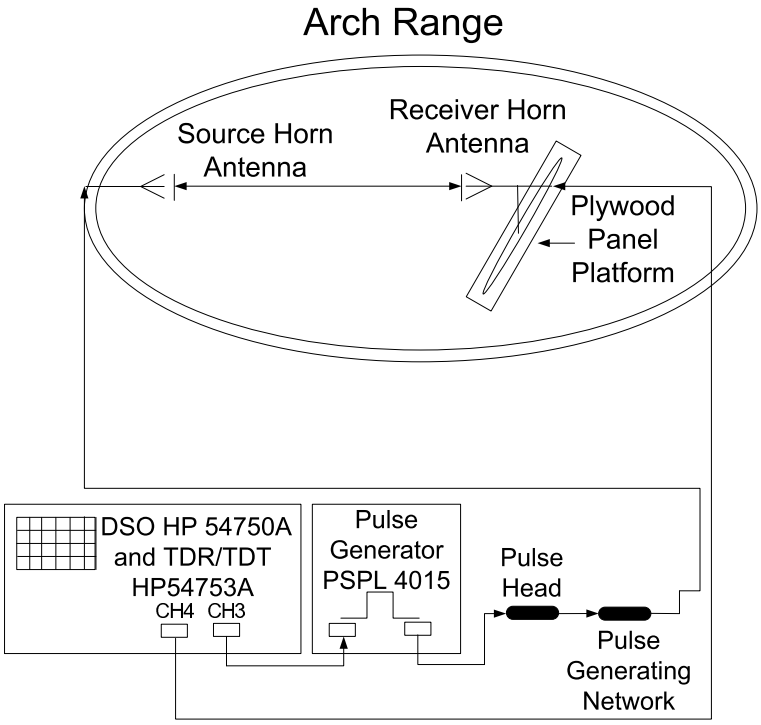

Figure 5.1: Experiment Set Up.

The time domain field detected by the receiving antenna is measured using a HP54750A Hewlett Packard digital sampling oscilloscope (DSO). The oscilloscope had a HP54753A vertical plug in module with a time-domain-reflectometer/time-domain-transmission (TDR/TDT) step generator built into channel 3. Channel 3, in the oscilloscope, has a 18 GHz bandwidth and channel 2 has a 20 GHz bandwidth. The (TDR/TDT) step generator produces a 200 mV step with a system rise time of 45 ps. These parameters are also presented in table 5.1. The HP 54753 triggers a Picosecond Pulse Labs (PSPL) pulse generator, model 4015 and the driver output is connected to a pulse head, model PSPL 4015RPH, that produces a -9V, 15 ps falltime

Figure 5.2: Transmitter antenna placed on the arch range.

Table 5.1: Oscilloscope Parameters.

Channel 3 Bandwidth	Channel 4 Bandwidth	Step Amplitude	Rise Time of Step Generator
18 GHz	20 GHz	200 mV	45ps

step pulse. The pulse head is connected to an impulse forming network, model PSPL 5208 DC, which receives the step and generates an approximately Gaussian pulse. This pulse is fed into the transmitting antenna. The voltage signal from the receiver antenna is applied by channel 4 on the oscilloscope. The signal was 4096 points long and the sampling time is 1.22 ps. The signal was averaged over 256 cycles to improve the SNR and the scale, on the oscilloscope was set to 3mV/div. The oscilloscope was turn on an hour before starting the experiment in order to avoid equipment thermal drift.

The receiver antenna was scanned using 3 cm step size to measure the electric field at 41 different positions over 120 cm distance, as shown in figures 5.6 and 5.7. The pulse was sent through the transmitter antenna every time the receiver antenna was moved to a different position. This procedure was followed because there was not an antenna array available. In order to maintain the receiver antenna from shifting to the sides a plywood panel was used. Two grooves were made on a plywood panel

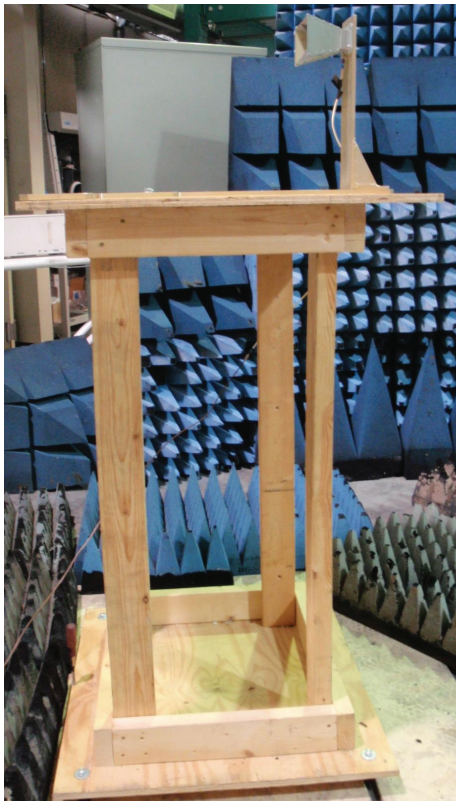

Figure 5.3: Receiver antenna on cart.

to guide the cart carrying the receiver antenna as shown in figure 5.8.

5.2 Experiment Calibration

A calibration procedure was followed to minimize the effects of different reflections from the room on the measurements. A conducting plate was placed between the transmitter antenna and the receiver antenna in order to measure the background clutter, as shown in figure 5.9. The background clutter includes reflections from the floor, ceiling, walls, and the metal arch range. Absorbers were placed on the floor, back walls, and in front of the cart, which holds the receiver antenna, to reduce the different reflections. After the background signal is obtained it is saved in the memory of the oscilloscope and subtracted from each signal measured along the linear scan positions of the receiver antenna.

(a)

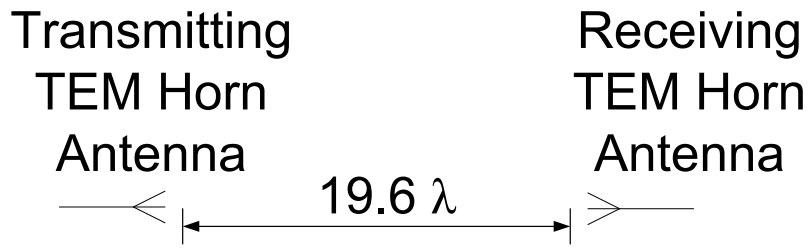

(b)

Figure 5.4: Experiment performed at a distance of 1.96 m between transmitter and receiver antennas. (a) Picture of experiment when antennas are 1.96 m away. (b) Drawing depicting the distance between the antennas.

5.3 Experiment Results

In the first experiment the distance between the transmitter antenna and the receiver antenna was 1.96 m. This distance was measured from the transmitter antenna to the receiver antenna placed in the center position. The field was measured in the x axis from -60 cm to 60 cm, as shown in figure 5.10. The signals, shown in figure 5.11, were decimated 4 times in order to input them into the FDTD model so that the value of Δt changed from 1.22 ps to 4.88 ps. The stability criteria was followed in the simulations ($c\Delta t \leq \frac{\Delta x}{\sqrt{2}}$) and the Δx was chosen to be 0.003 m. The decimated voltage signals were time reversed and used as input to the FDTD model using the experimental distance of 1.96 m from the source location.

The energy of the electric field in the back propagated electric field is calculated using the FDTD model. The position where the energy maximum occurs is estimated. The energy image in figure 5.12, shows the position where back propagated fields focus

(a)

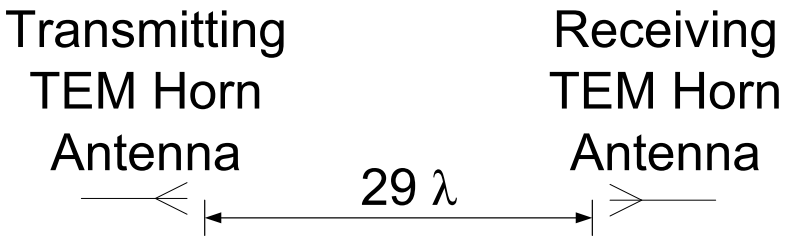

(b)

Figure 5.5: Experiment performed at a distance of 2.90 m between transmitter and receiver antennas. (a) Picture of experiment when antennas are 2.90 m away. (b) Drawing depicting the distance between the antennas.

on the source. Figure 5.12 shows the error between true (0,0) and estimated source location coordinates. The experiment was repeated at 2.90 m in order to reproduce the same error at a different distance and understand the source of the error. The electric field recorded for 41 different receiver positions is shown in figure 5.13. The energy image in figure 5.14, shows a similar error in the estimation of the source locations.

In order to understand the error in source location the experimental and simulated signals were analyzed. It was observed that the simulated signals at the first and last sensors positions were symmetric about the center position of receiver but this was not true of experimental signals. Experimental signals from positions -60 cm and 60

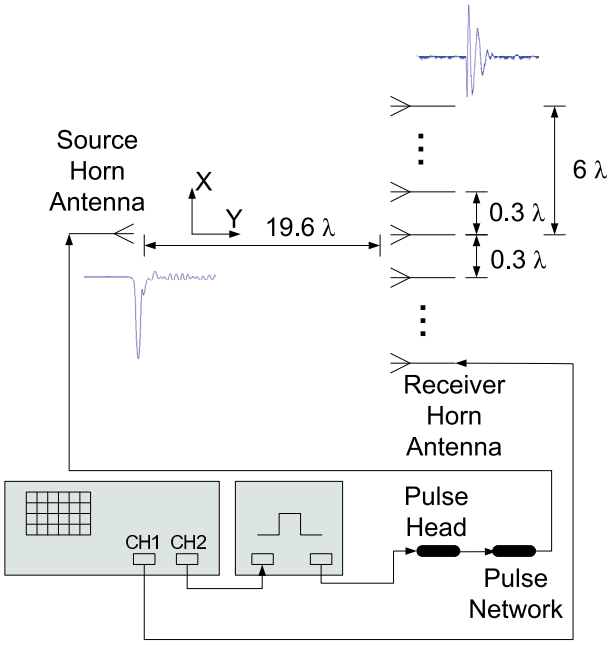

Figure 5.6: Experiment set up when antennas are 1.96m away.

cm in the x axis, for example, were compared and they were not identical, as shown in figure 5.15. It is observed in figure 5.15 that signal at position 60 cm has a shorter time delay than the signal at -60 cm. Theoretically this means that the distance between the receiver antenna and transmitter antenna at position 60 cm is shorter than the distance between the transmitter antenna and receiver antenna at position -60 cm. The difference in the values of the time of flight of signals at 60 cm and -60 cm were subtracted and the velocity of the wave in free space ($3 \times 10^8 m/s$) was used to find that the difference between the two sensors positions was 0.04 m. The distances between the transmitter and receiver antenna were measured for positions 60 cm and -60 cm in the experiment set up. The distance between transmitter and receiver antenna at position 60 cm is 2.9464 m and at position -60 cm the distance was measured as to be 2.9972 m, producing a difference of 0.0508 m which is close to the estimated error in distance between transmitter and receiver. The source of error is in estimation of source location is therefore attributed to the error in receiver location between simulation and experiment.

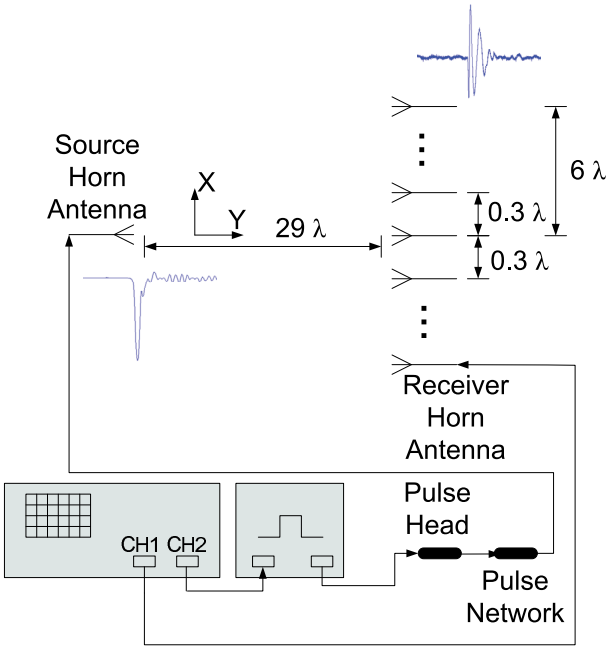

Figure 5.7: Experiment set up when antennas are 2.90m away.

The true distance was used next in the simulation in order to replicate the error shown in the experiments. A geometrical analysis was conducted to determine the location of the source. The distances that were measured in the experimental set up were used in this analysis. A triangulation method was used, as shown in figure 5.16.

The value of H was expected to represent the shortest distance between transmitter and receiver and intersect cathetus C in the middle or at 0 m. In the experimental set up, the distance between the transmitter and receiver was measured to be 2.9015 m. The difference in the measurements between catheti A and B caused the value of H to be different from the distance measured in the experiment set up. In addition, cathetus H does not intercept cathetus C in the middle as shown in figure 5.16.

Triangle formed by catheti B, H, and X1 shown in figure 5.17 is further analyzed. The Y cathetus is drawn from the source position to the point where catheti C from the triangle in figure 5.16 is divided in half. Catheti Y is found using Pythagoras theorem and it divides catheti X1 in X3=0.6 m and X4=0.099 m. The waves focused

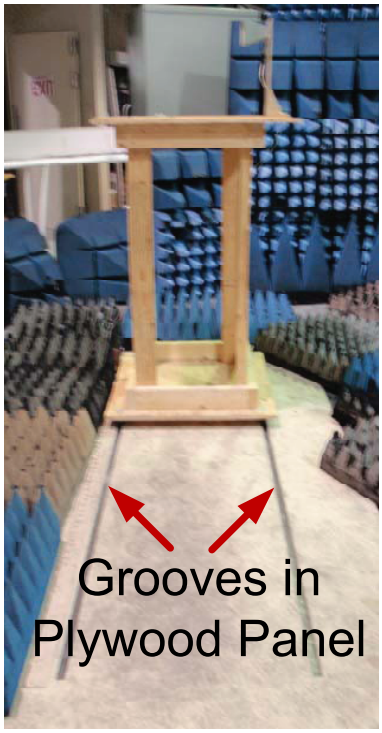

Figure 5.8: Plywood panel used to move and avoid shift in the receiver antenna.

at position (0.0920, -0.3850) when the experimental data was applied as input into the FDTD model. Distance X4=0.099 corresponds to the x coordinate where focusing occurred when the experimental data was used as input in the FDTD model. The difference in the distances of catheti A and B in figure 5.16 explains the error in the x coordinate.

The triangle in figure 5.18 is used to find the real position of the sensors in the experimental set up and to calculate the fields at this positions in the simulation. The triangle formed by catheti a1, b1, and d1 is a right triangle and trigonometric theorems are used to find b1. Coordinate b is found to be 2.929 by adding catheti b1 and Y. Cathetus d1 is found using trigonometric theorems and it also corresponds to coordinate a. The distance between coordinates (0,0) and coordinate (-0.5996,2.929) is found to be 2.99 m which is the same distance that was measured in the experimental set up. The same procedure was followed to find coordinates (0.5996,2.888). The distance between coordinates (0,0) and (0.5996,2.888) is found to be 2.94 m which

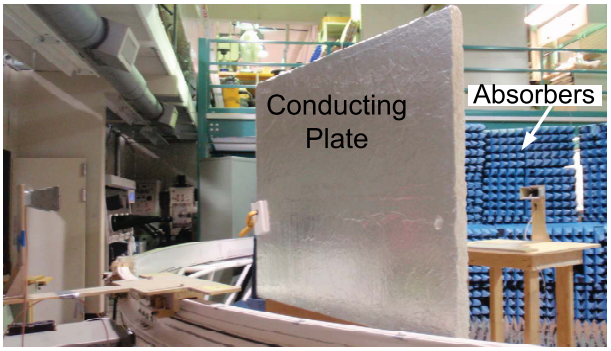

Figure 5.9: Conducting plate placed between transmitter and receiver antenna.

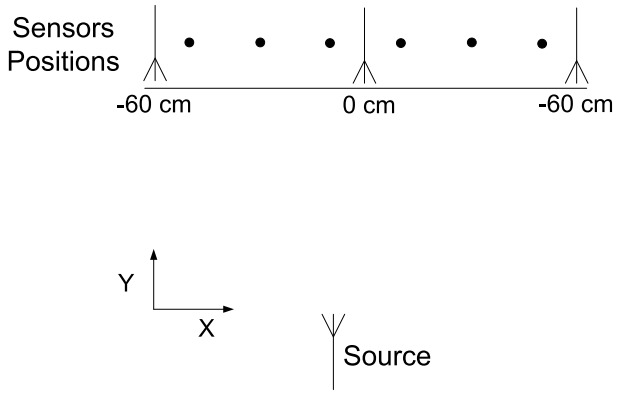

Figure 5.10: Electric field at sensors 1 to 41 for experiment where transmitter antenna is 1.96 m away from receiver antenna.

is the same distance that was measured in the experimental set up. The distance between coordinates (-0.5996,2.929) and (0.5996,2.888) was found to be 1.2 m which is the same distance that was covered by the receiver antenna.

Simulations replicating the experiment conditions were conducted to confirm that the asymmetry in experimental measurements at positions 60 cm and -60 cm were responsible for the error in estimation of source location. A gaussian modulated pulse with 2.8 GHz center frequency, was propagated in free space in the simulation. The 41 receivers were located at 17 different positions in the y axis, at a distance of 2.883 m to 2.931 m away from the source. The signals saved in the 17 different positions, were interpolated to find the signals on the line between coordinates (-0.5996,2.929) and (0.5996,2.888) in figure 5.18. These signals were then time reversed and propagated.

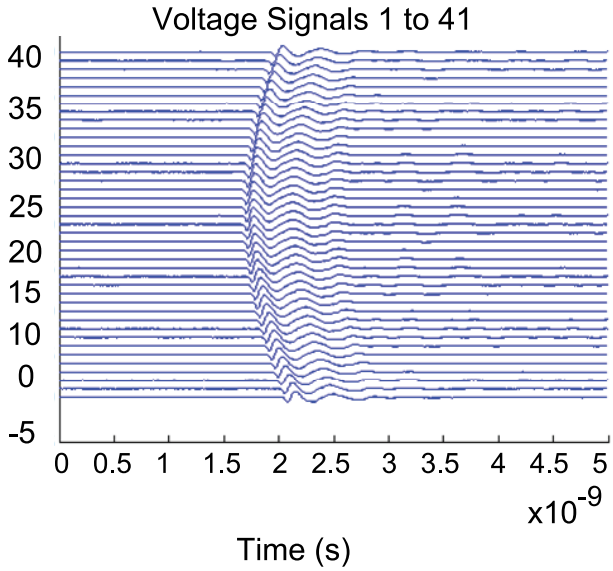

Figure 5.11: Electric field at sensors 1 to 41 for experiment where transmitter antenna is 1.96 m away from receiver antenna.

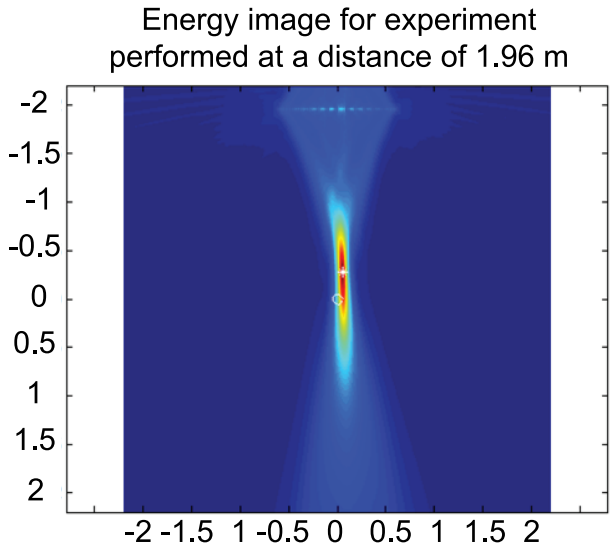

Figure 5.12: Energy image for experiment performed at a distance of 1.96 m where the energy maximum occurs at (0.053, -0.2740).

The energy image, in figure 5.19, shows the coordinates where the waves focuses. The wave, using data from the simulation, focuses at coordinates (0.080,-0.55), while when the experimental data is used, the wave focuses at coordinates (0.0920,-0.3850). The focusing error, caused by a difference in the distance between the transmitter and receiver at position 60 cm and -60 cm, was replicated.

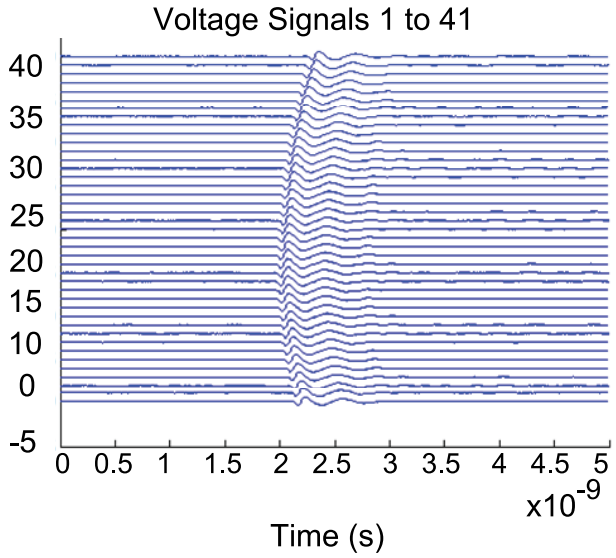

Figure 5.13: Electric field at sensors 1 to 41 for experiment where transmitter antenna is 2.90 m away from receiver antenna.

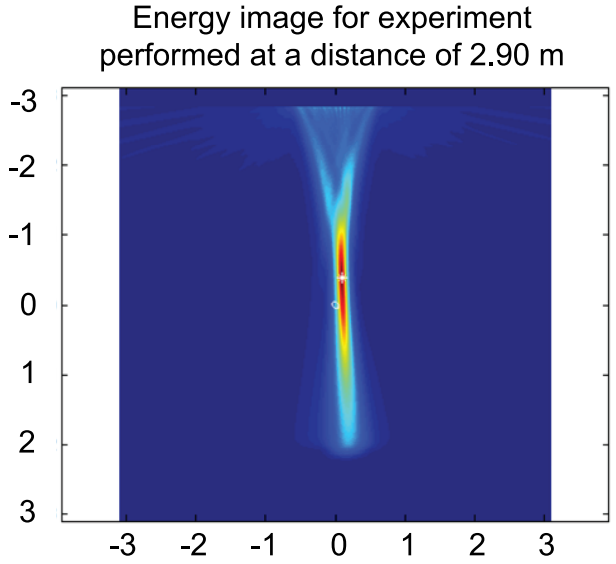

Figure 5.14: Energy image for experiment performed at a distance of 2.90 m where the energy maximum occurs at (0.0920, -0.3850).

The same procedure was followed in order to explain the source location error obtained when the experiment was performed at a distance of 1.96 m. The experimental signals at position 60 cm and -60 cm, shown in figure 5.20, are not identical. Signal 1 has a shorter time delay than signal 41. The time of flight of the peak in signal 1 is 2.034 ns and in signal 41, is 2.148 ns. The difference between the two is

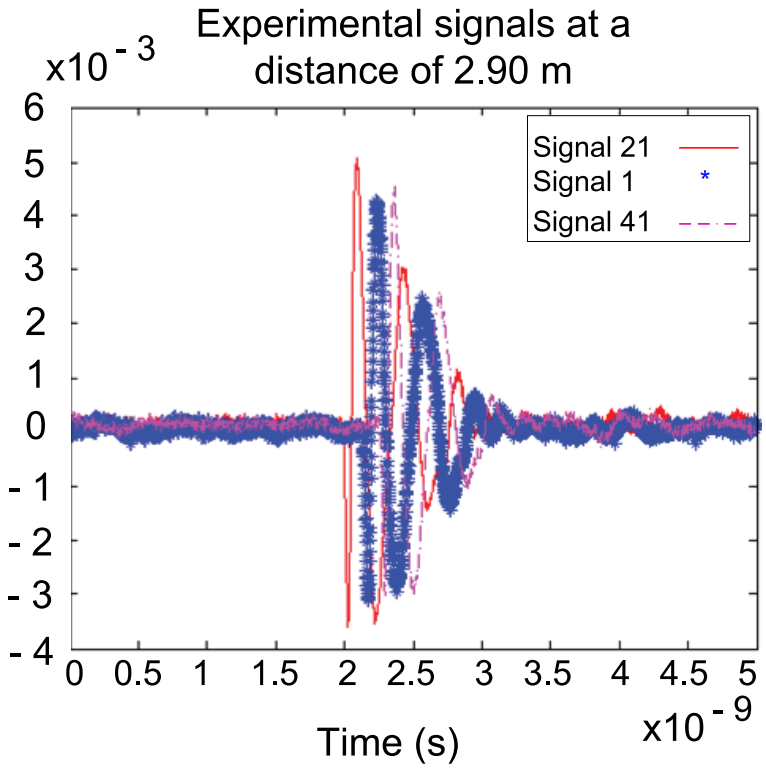

Figure 5.15: Experimental signals at a distance of 2.90 m for positions 1 (60 cm), 21 (0 cm), and 41 (-60 cm).

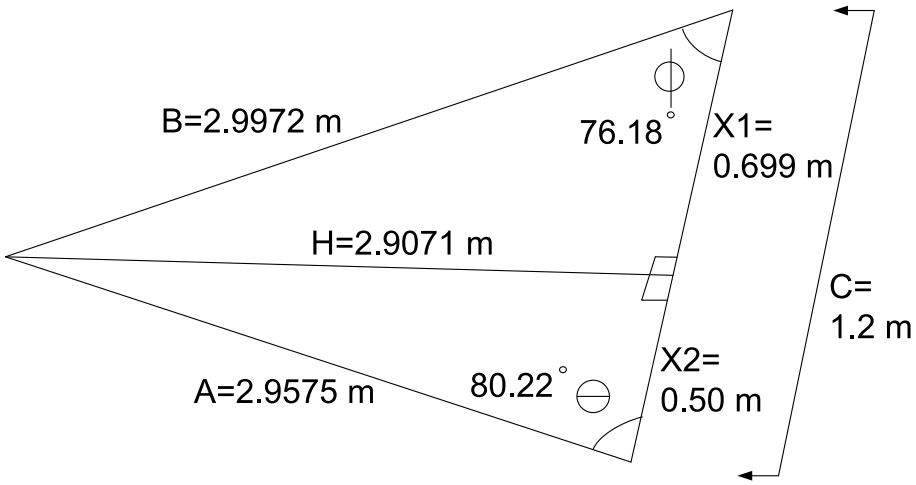

Figure 5.16: Triangle formed by the measurements taken at the experiment set up.

0.114 ns, which multiplied by the velocity of the wave in free space, yields a distance of 0.034 m. Triangulation techniques were used once again to explain the focusing error, as shown in figures 5.21, 5.22, and 5.23, to find the coordinates of the line

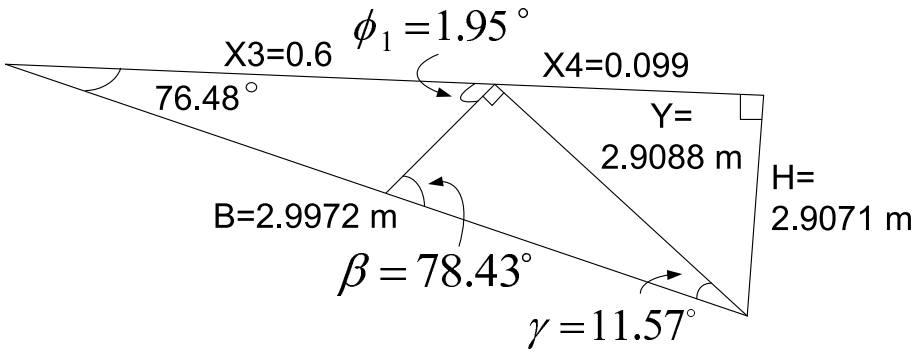

Figure 5.17: Triangle formed by the measurements taken at the experiment set up.

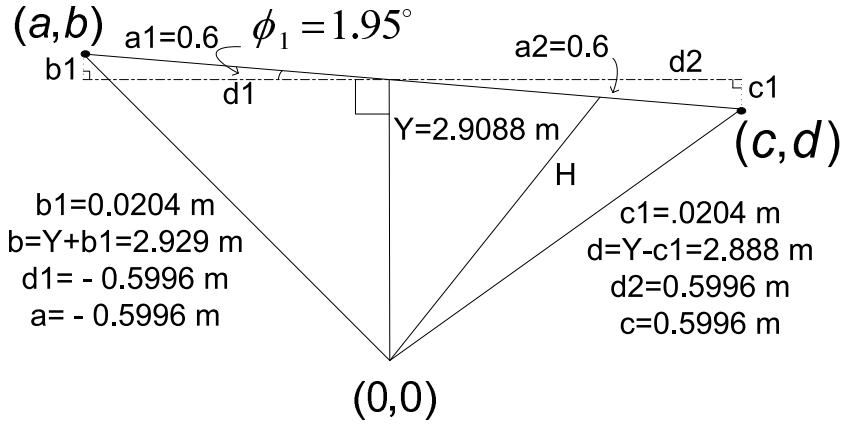

Figure 5.18: Triangle constructed to calculate coordinates of true sensors positions at the experiment set up.

where the 41 sensors lie. Cathetus Y=1.9776 m, shown in figure 5.22, corresponds to the shortest distance between transmitter and receiver. This distance is different from the measured distance of 1.96 m. Distance X4=0.06 m, shown in figure 5.22, is the distance between catheti Y and H and corresponds to the error found, in the x coordinate, when using the experimental data in the FDTD model. The error in the x coordinate was 0.0530 m which is similar to X4. The coordinates, where the linear array of sensors was placed, were found to be (-0.5997,-1.9949) and (0.5997,-1.96) as shown in figure 5.23. The distance between these coordinates was found to be 1.2 m, which corresponds to the distance measured in the experiment set up.

Simulations were performed to validate the FDTD model and replicate the error in the experiment. The 41 receivers were located at 15 different positions in the y

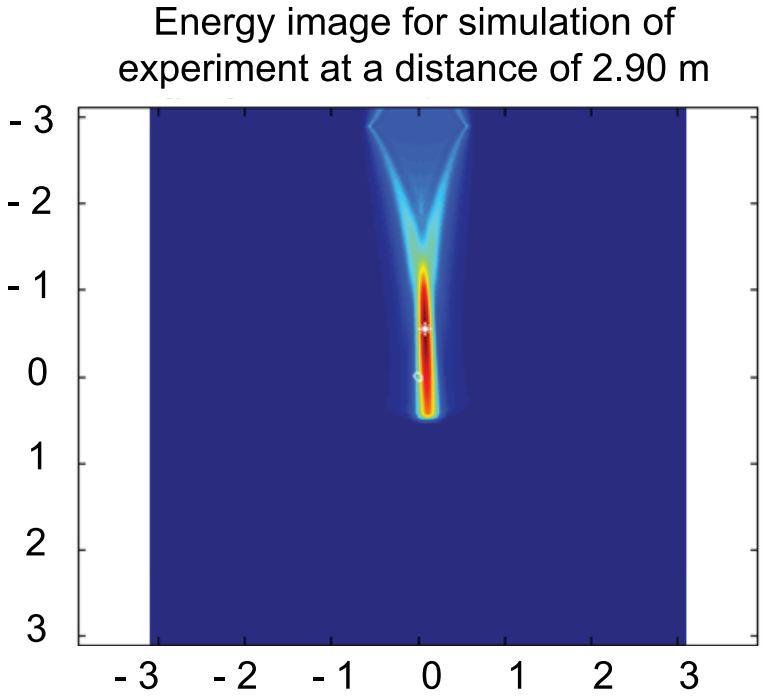

Figure 5.19: Energy image from simulation of experiment set up.

axis, at a distance of 1.96 m to 1.99 m away from the source. The signals, saved in the 15 different positions, were interpolated to find the signals on the line between coordinates (-0.5997,-1.9949) and (0.5997,-1.96) in figure 5.23. These signals were then time reversed and propagated. The energy image, in figure 5.24, shows the coordinates where the waves focus. The wave, using data from the simulation, focuses at coordinates (0.0500,-0.2050), while when the experimental data is used, the wave focuses at coordinates (0.0530,-0.2740). The focusing error, caused by a difference in the distance between the transmitter and receiver at position 60 cm and -60 cm, was replicated.

The experimental results presented in this chapter validates the concept of time reversal presented earlier using simulation signals. As expected the estimation of source location was in error. But the error was analyzed in detail and traced back to errors in experimental measurements. It should also be noted that the experimental geometry is three dimensional, whereas the FDTD model was only two dimensional.

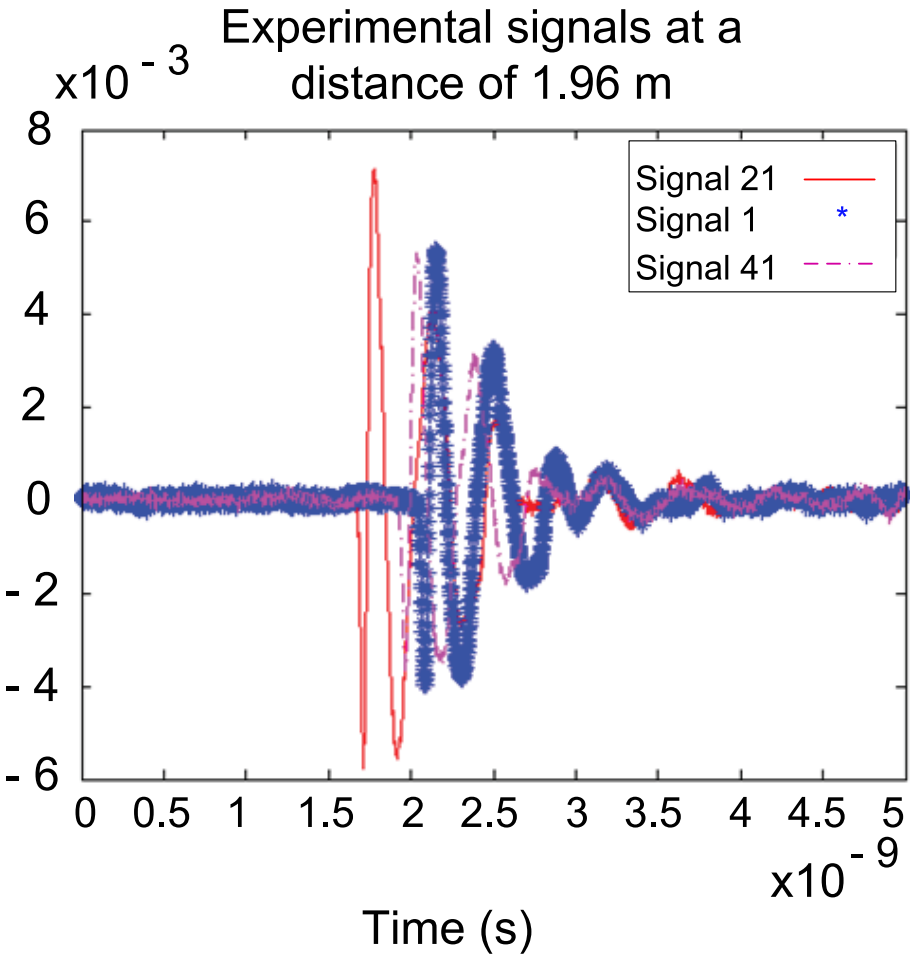

Figure 5.20: Experimental signals at a distance of 1.96 m for positions 1 (60 cm), 21 (0 cm), and 41 (-60 cm).

This is also expected to contribute in error in source location. However the results presented in this chapter clearly show that the experimental microwave NDE data can be used in conjunction with simulation model to reconstruct the position of source or defect in samples.

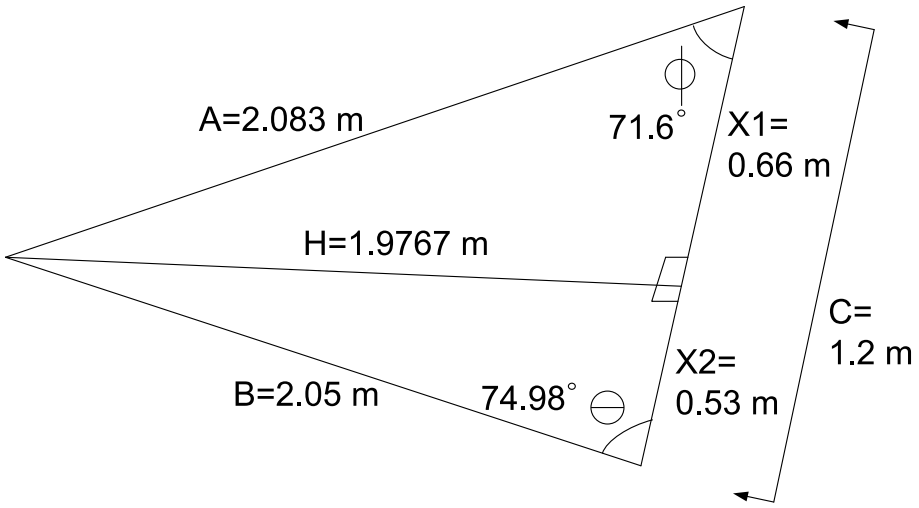

Figure 5.21: Triangle formed by the measurements taken at the experiment set up.

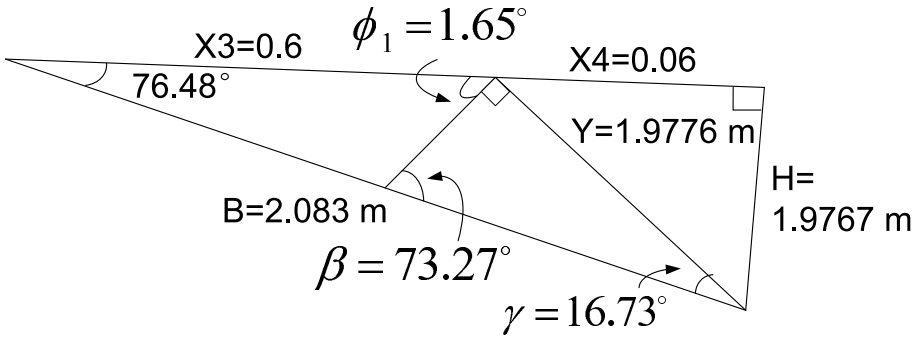

Figure 5.22: Triangle formed by the measurements taken at the experiment set up.

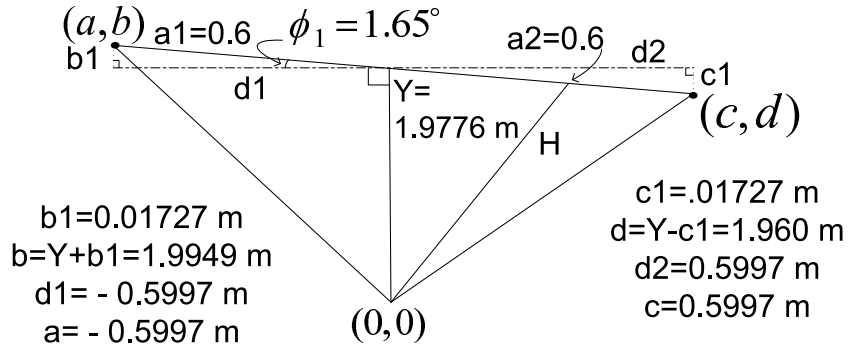

Figure 5.23: Triangle constructed to calculate coordinates of true sensors positions at the experiment set up.

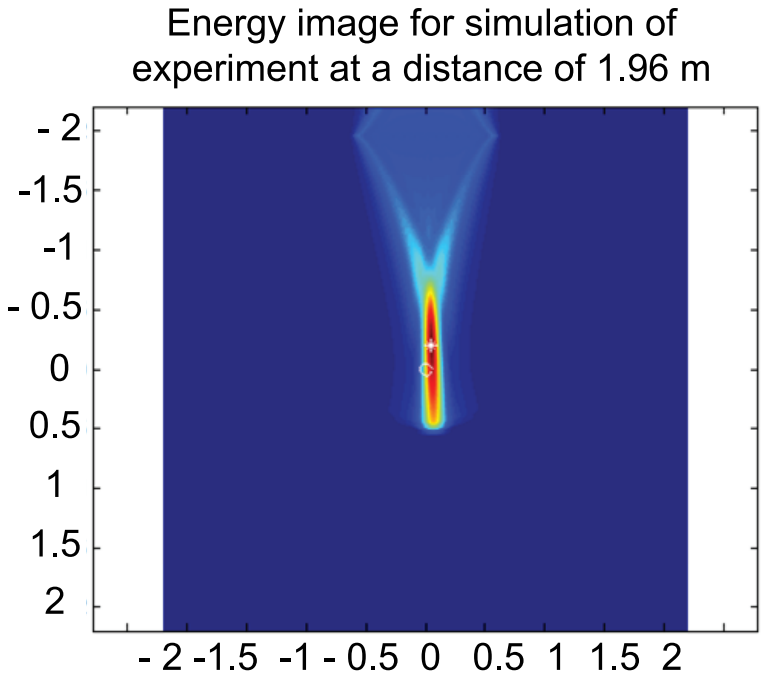

Figure 5.24: Energy image from simulation of experiment set up.

Chapter 6

Conclusions

In this dissertation we have proposed a model based inversion procedure, using principles of time reversal, for microwave NDE data. The formulation and simulation results, demonstrating the feasibility of the approach, are described. A computational FDTD model, for microwave NDE has been developed. The model has been used in conjunction with time reversal principles to solve the inverse problem. The most important contribution of this work is that it offers a model-based inverse problem solution in a non-iterative manner.

Simulations, testing the feasibility of the technique to detect single and multiple defects in dielectric and lossy dielectric materials, were performed. Defects were detected in lossy dielectric materials with conductivity values up to σ=0.1. The resolution of the technique was also tested. The model was used to distinguish two defects that were next to each other. Time reversal techniques were able to detect defects that were 2.27λ apart. The technique is robust in presence of measurement noise. Random noise with SNR=10 and 2 was added to the signals measured by the linear array. Energy images provided accurate information about the defect location for all the different simulations. The error between the coordinates of maximum energy and true locations of defects coordinates was small in all the simulations that

were performed.

Simulations, using different sensor locations and different distances between the source and sensor array, were performed in order to document the performance under different spatial distributions of sensors. Source detection was affected by the sensor locations because wave characteristics of the data were not captured when the receiver array covered a small area on the receiver plane. The distance between source and receiver array did not affect source detection. Different distance configurations between source and central receiver were used in the simulations. The source position was detected for all different distance configurations. The time delay of different signals was modified to document a source of error of the experiment. Source detection errors were higher when the time delay of the signals was modified. Time delay caused by errors in sensor positions did not affect source detection.

The FDTD model, used to solve the inverse problem of defect detection, was validated using experimental data. Errors were found in the estimation of the source location. The errors were attributed to the experimental measurements. Microwave NDE data and the FDTD model can be used to find defects and source locations.

Chapter 7

Future Work

This dissertation presents a non-iterative solution to the inverse problem of defect detection using the FDTD model and time reversal microwave techniques. Simulation results demonstrated the ability of the technique to accurately detect defects in dielectric and lossy dielectric materials. Simulations to characterize air voids in dielectric materials, using the FDTD model and time reversal techniques, will be performed. Several studies remain to be conducted.

- Energy images must be further analyzed using image processing techniques to determine size and shape of defects.

- Detection and characterization of disbonds or delaminations in composite materials using the FDTD model and time reversal techniques must be explored. The delaminations or disbonds can be simulated as extended defects. Energy images can be analyzed to determine size and shape of the defects.

- Simulation results showed that source or defect location is affected by the spatial distribution of the sensor array. Simulations using a narrower pulse can be performed to investigate if less sensor area can yield accurate determination of source location.

- Experiments, in free space, were performed to validate the FDTD model. Experiments, using samples with defects, must be performed to further validate the approach. Advanced algorithms that use experimental data in conjunction with the FDTD model to reconstruct the position of the defects in the sample, must be developed.

BIBLIOGRAPHY

BIBLIOGRAPHY

[1] S. Kharkovsky and R. Zoughi, "Microwave and millimeter wave nondestructive testing and evaluation - overview and recent advances," *IEEE Instrumentation Measurement Magazine*, vol. 10, no. 2, pp. 26 –38, Apr. 2007.

[2] K. Bois, L. Handjojo, A. Benally, K. Mubarak, and R. Zoughi, "Dielectric plug-loaded two-port transmission line measurement technique for dielectric property characterization of granular and liquid materials," *IEEE Transactions on Instrumentation and Measurement*, vol. 48, no. 6, pp. 1141 –1148, Dec. 1999.

[3] R. Zoughi, *Microwave Non-Destructive Testing and Evaluation Principles*. Springer, 2000.

[4] D. Shreiber, M. Gupta, and R. Cravey, "Microwave nondestructive evaluation of dielectric materials with a metamaterial lens," *Sensors and Actuators A: Physical*, vol. 144, no. 1, pp. 48 – 55, 2008.

[5] S. Kharkovsky, M. Akay, U. Hasar, and C. Atis, "Measurement and monitoring of microwave reflection and transmission properties of cement-based specimens," *IEEE Transactions on Instrumentation and Measurement*, vol. 51, no. 6, pp. 1210 – 1218, Dec. 2002.

[6] K. Arunachalam, V. Melapudi, L. Udpa, and S. Udpa, "Microwave ndt of cement-based materials using far-field reflection coefficients," *NDT/E International*, vol. 39, no. 7, pp. 585 – 593, 2006.

[7] K. Bois, A. Benally, and R. Zoughi, "Microwave near-field reflection property analysis of concrete for material content determination," *IEEE Transactions on Instrumentation and Measurement*, vol. 49, no. 1, pp. 49 –55, Feb. 2000.

[8] S. Kharkovsky, A. Wang, T. Case, and R. Zoughi, "Dual-polarized near-field microwave reflectometer for noninvasive inspection of carbon fiber reinforced polymer-strengthened structures," *IEEE Transactions on Instrumentation and Measurement*, vol. 57, no. 1, pp. 168 –175, Jan. 2008.

[9] D. Hughes, N. Ryley, V. Stephen, K. Donnell, R. Zoughi, R. Austin, and M. Novack, "Microwave nondestructive detection of corrosion under thin paint and primer in aluminum panels," *Subsurface Sensing Technologies and Applications*, vol. 2, no. 4, pp. 435 –471, Oct. 2001.

[10] N. Qaddoumi, A. Shroyer, and R. Zoughi, "Microwave detection of rust under paint and composite laminates," *Research in Nondestructive Evaluation*, vol. 9, no. 4, pp. 201 – 212, 1997.

[11] H. K. Sezer, L. Li, Z. Wu, B. Anderson, and P. Williams, "Mechanisms of acute angle laser drilling induced thermal barrier coating delamination," *Journal of Manufacturing Science and Engineering*, vol. 131, no. 5, p. 051014, 2009.

[12] A. V. Joshi, "Inverse problems in non-destructive evaluation of gas transmission pipelines using magnetic flux leakage," Ph.D. dissertation, Michigan State University, 2006.

[13] S. Hoole, S. Subramaniam, R. Saldanha, J.-L. Coulomb, and J.-C. Sabonnadiere, "Inverse problem methodology and finite elements in the identification of cracks, sources, materials, and their geometry in inaccessible locations," *IEEE Transactions on Magnetics*, vol. 27, no. 3, pp. 3433 –3443, may 1991.

[14] H. A. Sabbagh, L. D. Sabbagh, and T. M. Roberts, "An eddy-current model and algorithm for three-dimensional nondestructive evaluation of advanced composites," *IEEE Transactions on Magnetics*, vol. 24, no. 6, pp. 3201 –3212, Nov. 1988.

[15] J. Hadamard, *Sur les problmes aux drives partielles et leur signification physique.* Princeton University Bulletin, 1992.

[16] P. Ramuhalli, L. Udpa, and S. S. Udpa, "Neural network-based inversion algorithms in magnetic flux leakage nondestructive evaluation," *Journal of Applied Physics*, vol. 93, no. 10, pp. 8274 –8276, May 2003.

[17] F. Wu, J.-L. Thomas, and M. Fink, "Time reversal of ultrasonic fields. II. experimental results," *IEEE Transactions on Ultrasonics, Ferroelectrics and Frequency Control*, vol. 39, no. 5, pp. 567 –578, Sep. 1992.

[18] R. Ing and M. Fink, "Time recompression of dispersive lamb waves using a time reversal mirror-application to flaw detection in thin plates," in *Ultrasonics Symposium, 1996. Proceedings., 1996 IEEE*, vol. 1, Nov. 1996, pp. 659 –663 vol.1.

[19] P. Kosmas and C. Rappaport, "Time reversal with the fdtd method for microwave breast cancer detection," *IEEE Transactions on Microwave Theory and Techniques*, vol. 53, no. 7, pp. 2317 – 2323, Jul. 2005.

[20] G. Lerosey, J. de Rosny, A. Tourin, A. Derode, G. Montaldo, and M. Fink, "Time reversal of electromagnetic waves," in *Physical Review Letters*, vol. 92, no. 19, May. 2004, pp. 193 904–1–193 904–3.

[21] K. Yee, "Numerical solution of initial boundary value problems involving maxwell's equations in isotropic media," *Antennas and Propagation, IEEE Transactions on*, vol. 14, no. 3, pp. 302 –307, May. 1966.

[22] A. Peterson, S. Ray, and R. Mittra, *Computational Methods for Electromagnetics.* IEEE Press, 1998.

[23] G. Mur, "Absorbing boundary conditions for the finite-difference approximation of the time-domain electromagnetic-field equations," *Electromagnetic Compatibility, IEEE Transactions on*, vol. EMC-23, no. 4, pp. 377 –382, Nov. 1981.

[24] P. Ramuhalli, L. Udpa, and S.Udpa, "Electromagnetic nde signal inversion by function-approximation neural networks," *IEEE Transactions on Magnetics*, vol. 38, no. 6, pp. 3633 – 3642, 2002.

[25] P. De Oliveira, F. Ramos, R. Garto, H. Velho, S. Stephany, P. Navarro, P. Husbands, and I. Harvey, "A research agenda for iterative approaches to inverse problems using evolutionary computation," in *Proceedings of IEEE International Conference on Evolutionary Computation, 1996.*, May 1996, pp. 55 –60.

[26] L. Udpa and S. Udpa, "Application of signal processing and pattern recognition techniques to inverse problems in nde," *International Journal of Applied Electromagnetics and Mechanics*, no. 8, pp. 99 – 117, 1997.

[27] M. Fink, "Time reversal of ultrasonic fields. i. basic principles," *IEEE Transactions on Ultrasonics, Ferroelectrics and Frequency Control*, vol. 39, no. 5, pp. 555 –566, Sep. 1992.

[28] P. Kosmas and C. Rappaport, "A matched-filter fdtd-based time reversal approach for microwave breast cancer detection," *IEEE Transactions on Antennas and Propagation*, vol. 54, no. 4, pp. 1257 – 1264, Apr. 2006.

[29] N. Chakroun, F. Wu, and M. Fink, "Improvement of time reversal mirror in detection of small cracks and metallurgical defects in sample with high ultrasonic speckle noise level," in *Ultrasonics Symposium, 1993. Proceedings., IEEE 1993*, Oct.-3 Nov. 1993, pp. 705 –710 vol.2.

[30] V. Miette, L. Sandrin, F. Wu, and M. Fink, "Optimisation of time reversal processing in titanium inspections," in *Ultrasonics Symposium, 1996. Proceedings., 1996 IEEE*, vol. 1, Nov. 1996, pp. 643 –647 vol.1.

[31] N. Chakroun, M. Fink, and F. Wu, "Time reversal processing in ultrasonic nondestructive testing," *IEEE Transactions on Ultrasonics, Ferroelectrics and Frequency Control*, vol. 42, no. 6, pp. 1087 –1098, Nov. 1995.

[32] T. Leutenegger and J. Dual, "Detection of defects in cylindrical structures using a time reverse method and a finite-difference approach," *Ultrasonics*, vol. 40, no. 1-8, pp. 721 – 725, 2002.

[33] ——, "Non-destructive testing of tubes using a time reverse numerical simulation (trns) method," *Ultrasonics*, vol. 41, no. 10, pp. 811 – 822, 2004.

[34] N. Dominguez, V. Gibiat, and Y. Esquerre, "Time domain topological gradient and time reversal analogy: an inverse method for ultrasonic target detection," *Wave Motion*, vol. 42, no. 1, pp. 31 – 52, 2005.

[35] J. Thomas, P. Roux, and M. Fink, "Inverse problem in wave scattering with an acoustic time-reversal mirror," in *Ultrasonics Symposium, 1993. Proceedings., IEEE 1993*, 31 1993, pp. 1143 –1148 vol.2.

[36] R. Carminati, R. Pierrat, J. de Rosny, and M. Fink, "Theory of the time reversal cavity for electromagnetic fields," *Opt. Lett.*, vol. 32, no. 21, pp. 3107–3109, 2007.

[37] D. Liu, G. Kang, L. Li, Y. Chen, S. Vasudevan, W. Joines, Q. H. Liu, J. Krolik, and L. Carin, "Electromagnetic time-reversal imaging of a target in a cluttered environment," *IEEE Transactions on Antennas and Propagation*, vol. 53, no. 9, pp. 3058 – 3066, sep. 2005.

[38] N. Maaref, P. Millot, X. Ferrires, C. Pichot, and O. Picon, "Electromagnetic imaging method based on time reversal processing applied to through-the-wall target localization," *Progress In Electromagnetics Research M*, vol. 1, pp. 59–67, 2008.

[39] C. Leuschen and R. Plumb, "A matched-filter-based reverse-time migration algorithm for ground-penetrating radar data," *Geoscience and Remote Sensing, IEEE Transactions on*, vol. 39, no. 5, pp. 929 –936, May. 2001.

[40] S. K. Lehman and A. J. Devaney, "Transmission mode time-reversal super-resolution imaging," *The Journal of the Acoustical Society of America*, vol. 113, no. 5, pp. 2742–2753, 2003.

[41] M. Fink and C. Prada, "Acoustic time-reversal mirrors," *Inverse Problems*, vol. 17, no. 1, p. R1, 2001.